Monthly Notices
of the
ROYAL ASTRONOMICAL SOCIETY

Mon. Not. R. Astron. Soc. **418,** 1071–1088 (2011) doi:10.1111/j.1365-2966.2011.19558.x

Luminous starbursts in the redshift desert at $z \sim 1$–2: star formation rates, masses and evidence for outflows

Manda Banerji,[1⋆] S. C. Chapman,[1] Ian Smail,[2] S. Alaghband-Zadeh,[1] A. M. Swinbank,[2] J. S. Dunlop,[3] R. J. Ivison[4,3] and A. W. Blain[5]

[1]*Institute of Astronomy, University of Cambridge, Madingley Road, Cambridge CB3 0HA*
[2]*Institute for Computational Cosmology, Durham University, South Road, Durham DH1 3LE*
[3]*Institute for Astronomy, University of Edinburgh, Royal Observatory, Edinburgh EH9 3HJ*
[4]*UK Astronomy Technology Centre, Royal Observatory, Blackford Hill, Edinburgh EH9 3HJ*
[5]*Department of Physics and Astronomy, University of Leicester, University Road, Leicester LE1 7RH*

Accepted 2011 August 1. Received 2011 August 1; in original form 2011 May 27

ABSTRACT

We present a spectroscopic catalogue of 40 luminous starburst galaxies at $z = 0.7$–1.7 (median $z = 1.3$). 19 of these are submillimetre galaxies (SMGs) and 21 are submillimetre-faint radio galaxies (SFRGs). This sample helps us to fill in the redshift desert at $z = 1.2$–1.7 in previous studies as well as to probe a lower luminosity population of galaxies. Radio fluxes are used to determine star formation rates for our sample which range from around 50–500 $M_\odot\,yr^{-1}$ and are generally lower than those in $z \sim 2$ SMGs. We identify nebular [O II] 3727 emission in the rest-UV spectra and use the linewidths to show that SMGs and SFRGs in our sample have larger linewidths and therefore dynamical masses than optically selected star-forming galaxies at similar redshifts. The linewidths are indistinguishable from those measured in the $z \sim 2$ SMG populations suggesting little evolution in the dynamical masses of the galaxies between redshift 1 and 2. [Ne V] and [Ne III] emission lines are identified in a subset of the spectra indicating the presence of an active galactic nucleus (AGN). In addition, a host of interstellar absorption lines corresponding to transitions of Mg II and Fe II ions are also detected. These features show up prominently in composite spectra and we use these composites to demonstrate that the absorption lines are present at an average blueshift of $-240 \pm 50\,km\,s^{-1}$ relative to the systemic velocities of the galaxies derived from [O II]. This indicates the presence of large-scale outflowing interstellar gas in these systems. We do not find any evidence for differences in outflow velocities between SMGs and SFRGs of similar infrared luminosities. We find that the outflow velocities of $z \sim 1.3$ SMGs and SFRGs are consistent with the $V \propto SFR^{0.3}$ local envelope seen in lower redshift ultraluminous infrared galaxies (ULIRGs). These observations are well explained by a momentum-driven wind model.

Key words: galaxies: high-redshift – galaxies: ISM – galaxies: starburst.

1 INTRODUCTION

Submillimetre (sub-mm) galaxies (SMGs) selected based on their 850-μm fluxes (Blain et al. 1999; Chapman et al. 2005; Coppin et al. 2006; Weiß et al. 2009) play an important role in the overall star formation history of the Universe. They are thought to be the high-redshift counterparts of the most infrared luminous systems in the local Universe such as the luminous infrared galaxies (LIRGs) and ultraluminous infrared galaxies (ULIRGs) and progenitors of the most massive ellipticals seen today (Swinbank et al. 2006, 2008). However, the sensitivity of current generation sub-mm instruments such as the Large Apex Bolometer Camera (LABOCA) biases the detection of SMGs to those with cooler dust temperatures, therefore missing a population of luminous but hotter starbursts at high redshifts. Sub-mm-faint radio galaxies (SFRGs) have been proposed as an extension of the SMG population to hotter dust temperatures (Chapman et al. 2004, 2010; Casey et al. 2009; Magnelli et al. 2010). Radio observations of SFRGs indicate that they are very similar to SMGs in terms of radio morphology and size (Casey et al. 2011). Together, these two populations have an SFR density at redshifts ∼1–3 that is roughly comparable to the rest-frame UV selected

⋆E-mail: mbanerji@ast.cam.ac.uk

population. These galaxies therefore represent a reasonably complete sample of infrared luminous galaxies at the main epoch of galaxy formation.

The most extensive spectroscopic sample of SMGs and SFRGs to date has been presented in Chapman et al. (2004, 2005) (C04 and C05 hereafter). This sample has a median redshift of 2–2.5 with a dip in the numbers below $z \sim 1.5$ where no strong spectral features fall into the Keck-LRIS (Low-Resolution Imaging Spectrometer) window used for redshift identification. Redshifts obtained from the rest-UV analysis of this prodigiously star-forming massive galaxy population, have motivated further observations of these galaxies at multiple wavelengths all the way from the X-ray (Alexander et al. 2005) through the infrared (Swinbank et al. 2004, 2010) to the millimeter (Tacconi et al. 2008). Such observations have been successful in constraining a wide range of physical parameters such as the active galactic nucleus (AGN) content, masses, sizes, morphologies and merging histories of these galaxies.

The rest-UV spectra themselves are rich in spectral features (Leitherer et al. 2011) that can be used to trace cool interstellar gas in the galaxies in order to look for signatures of outflows. Provided that one can obtain a reasonable estimate of the systemic redshift of the galaxies, numerous absorption lines in the rest-UV can be used to probe the state of the cool atomic gas and characterize *feedback* processes in the galaxies. A wealth of observational evidence now suggests that galactic winds are in fact ubiquitous in galaxies with star-formation surface density, $\Sigma_{\rm SF} \gtrsim 10^{-1}\,{\rm M}_{\odot}\,{\rm yr}^{-1}\,{\rm kpc}^{2}$ (Heckman, Armus & Miley 1990) and the most powerful starbursts can power winds that are approaching the escape velocity of the galaxy. Winds that can escape the galaxy are likely to be responsible for the metal enrichment of the IGM and the observed mass–metallicity relation of galaxies (Tremonti et al. 2004; Erb et al. 2006; Maiolino et al. 2008).

There have been extensive studies of galactic-scale outflows in local starbursts ranging from dwarfs (Schwartz et al. 2006) to LIRGs and ULIRGs (Heckman et al. 2000; Rupke, Veilleux & Sanders 2002; Martin 2005). Recently, Weiner et al. (2009) and Rubin et al. (2010) extended this analysis to optically selected star-forming galaxies at $z \sim 1.5$ using stacked spectra from the DEEP2 survey to demonstrate that outflows are also ubiquitous at high redshifts. At even higher redshifts, studies of the most luminous Lyman break galaxies also show signs of outflowing gas in these systems (Pettini et al. 2001, 2002; Shapley et al. 2003; Steidel et al. 2010) and outflow velocities of several hundred $\rm km\,s^{-1}$ have been measured in lensed Lyman α emitting systems (Frye, Broadhurst & Benítez 2002).

The Keck-LRIS spectra in C04 and C05 did not allow for a study of galactic-scale outflows due to the lack of suitable spectral features for systemic redshift determination at the observed wavelengths. However, numerous individual sub-mm-detected galaxies have been studied in detail and shown to drive powerful outflows. These include N2 850.4 (Smail et al. 2003; Swinbank et al. 2005) which shows blueshifted Si II and Ca II interstellar absorption features with a velocity of $700\,\rm km\,s^{-1}$. Alexander et al. (2010) use integral field spectroscopy to identify a highly energetic outflow from the sub-mm galaxy SMM J1237+6203 at $z \sim 2$ being radiatively powered by AGNs and/or supernovae. Similarly, Nesvadba et al. (2007) also show that the lensed starburst SMM J14011+0252 at $z \sim 2.6$ is powering a superwind with a velocity of 350–$500\,\rm km\,s^{-1}$.

Motivated by these previous studies, our objective in the current paper is therefore two-fold. First, we present a spectroscopic catalogue of SMGs and SFRGs observed using the Keck-II DEep Imaging Multi-Object Spectrograph (DEIMOS) spectrograph with a view to filling in the *redshift desert* at $z < 1.5$ in the C04 and C05 samples. Our galaxies have lower redshifts and lower characteristic luminosities compared to these previous studies, thus helping us to characterize both the redshift and luminosity evolution of SMG/SFRG properties. The wavelength window of the DEIMOS spectrograph allows us to identify nebular [O II] 3727 emission, which can be used to determine the systemic redshifts of the galaxies as the warm ionized gas from which this emission originates is associated with young stars. The rest-UV spectra therefore also allow us to search for signatures of outflowing gas in the galaxies in order to compare to both the local starbursts and the optically selected star-forming galaxies at redshifts similar to our sample.

The paper is structured as follows. Section 2 describes our sample selection, spectroscopic observations, galaxy properties derived from broad-band photometry and creation of composite spectra. In Section 3 we present the main results of our spectroscopic study including characterization of the [O II] line profiles in the galaxies and derivations of outflow velocities and their dependence on galaxy properties. We discuss these trends in Section 4. Finally in Section 5 we give our conclusions. Throughout this paper we assume a flat Λ cold dark matter (ΛCDM) cosmology with $\Omega_{\rm m} = 0.3$, $\Omega_{\Lambda} = 0.7$ and $h = 0.7$. All magnitudes quoted are on the AB system.

2 OBSERVATIONS

We begin with a description of our sample selection and the spectroscopic observations.

2.1 Sample selection

C05 have presented the most extensive catalogue of SMG redshifts to date with the selection criteria aimed at identifying the bulk of the SMG population brighter than $S_{850} = 5\,\rm mJy$. The redshift distribution for these galaxies peaks around $z \sim 2$–2.5 with a dip in the numbers below $z \sim 1.5$ due to Keck-LRIS's spectral coverage. Hotter dust counterparts to these galaxies have also been presented in C04 spanning similar redshifts. With the aim of filling in the *redshift desert* in these samples, a redshift survey was carried out using the red-sensitive Keck-II DEIMOS (Faber et al. 2003) in order to target emission-line galaxies at $z \sim 1.3$ predominantly through their [O II] 3727 emission. The survey was carried out in four fields – Hubble Deep Field North (HDF-N), Lockman Hole, Subaru/XMM-Newton Deep Field (SXDF) and the 03h field in the Canada France Redshift Survey (CFRS03). All the targeted galaxies have robust detections in the radio, 850-μm fluxes from SCUBA/JCMT (see Table 2) or are detected in *Herschel* SPIRE catalogues at 250–500 μm (Chapman et al. 2010). Radio data in the Lockman Hole are taken from Ivison et al. (2002) and Ivison et al. (2007) who identified the counterparts to the sub-mm galaxies in these regions from Coppin et al. (2006). The radio data for SXDF are from a deeper map from Arumugam et al. (in preparation) and the sub-mm counterparts are again identified from Coppin et al. (2006). The sub-mm and radio data in the CFRS03 field are taken from Webb et al. (2003). Radio data in the HDF have been presented in Biggs & Ivison (2006) and Morrison et al. (2010) and sub-mm detections in this field are taken from Borys et al. (2002).

2.2 Spectroscopic observations

Spectroscopic observations were made with the Keck-II DEIMOS spectrograph on 2003 December 23, 2005 October 8–9, and 2005

Table 1. Summary of various composite spectra analysed in this study including the number of galaxies comprising them and their continuum S/N at 2700 Å.

	$N_{\rm gal}$	S/N at 2700 Å
All [no e(a)]	26	6.6
All [incl. e(a)]	31	7.7
SMG	13	6.0
SFRG	13	3.9
AGN	15	4.7
SF	16	4.9
$L_{\rm IR} > 1.09 \times 10^{12}\,{\rm L}_{\odot}$	12	4.8
$L_{\rm IR} < 0.65 \times 10^{12}\,{\rm L}_{\odot}$	10	3.7
12+log(O/H)>8.4 (Low [Ne III]/[O II])	15	4.7
12+log(O/H)<8.2 (High [Ne III]/[O II])	10	5.2
$\log_{10}(M_*/{\rm M}_{\odot}) > 10.80$	11	4.7
$\log_{10}(M_*/{\rm M}_{\odot}) < 10.50$	11	5.5
$\log_{10}(M_{\rm dyn}/{\rm M}_{\odot}) > 10.50$	13	3.5
$\log_{10}(M_{\rm dyn}/{\rm M}_{\odot}) < 10.30$	13	6.3

February 22 (with seeing ranging from 0.6 to 1.0 arcsec) and the full sample of $z \sim 1.3$ galaxies with spectroscopic redshifts is presented in Table 2. The lower resolution mode was used in all cases to gain the widest wavelength coverage, with a grating of 600 line mm^{-1} yielding a resolution of 3 Å or $\sim$100 km s^{-1} (measured from the sky lines) and a scale of 0.65 Å pixel^{-1}. For a slit in the middle of the mask the observed wavelength range was 5600–9800 Å. The [O II] doublet is only moderately resolved in a handful of spectra in this setting and this and other red spectral features studied can be affected by proximity to the strong night sky OH recombination lines. All data were reduced using the DEIMOS-DEEP2 pipeline (Faber et al. 2003).

The candidate redshifts in all cases are based on the identification of [O II] 3727 emission in the 2D spectra. In most cases, the redshift is then corroborated through identification of multiple emission and absorption lines, including subsets of Fe II(2344, 2374, 2383, 2586, 2600 Å), Mg II (2803, 2853 Å), Hδ (4103 Å), Hγ (4340 Å) and Ca H&K (3933, 3969 Å) in absorption, and [Ne III] (3869 Å), [Ne V] (3426 Å) and [O III] (4959, 5007 Å) in emission. The DEIMOS coverage allows us to target emission lines in galaxies between $z = 0.7$ and 1.7. In this redshift range, the spectroscopic completeness is estimated to be $\sim$70 per cent from the fraction of radio IDs in the different masks with well-detected spectral features.

Redshifts are measured by fitting two Gaussians of equal width and intensity centred at 3726.1 and 3728.8 Å to the blended [O II] line observed in most of the spectra. The [O II] redshift errors estimated from adjusting the Gaussian fits to give $\Delta\chi^2 = 1$ are of the order of 60 km s^{-1}.

As much of the paper is concerned with characterizing velocity offsets of interstellar absorption lines from [O II], it is important to devise a sensible method of measuring the centroids and widths of the absorption lines. The absorption line profiles are often highly asymmetric with large velocity tails and it is therefore not appropriate to fit Gaussians to the line profiles. The velocities and equivalent widths are instead calculated by measuring the line centroids according to the apparent optical depth (AOD) formalism of Savage & Sembach (1991).

Errors in the [O II] redshift estimates, poor wavelength calibration at the blue-end of the spectrum and poor signal-to-noise ratio (S/N) could all lead to systematic differences between the [O II] and interstellar absorption line redshifts. Redshift errors arising from the Gaussian fits to the [O II] line have already been discussed. There are five examples of spectra where, in addition to [O II], several other emission lines such as [O III], [Ne III], [Ne V] and various Balmer absorption features are also detected. We find these features to be shifted by $+10 \pm 80$ km s^{-1} relative to [O II]. This shift is within the typical redshift error associated with the Gaussian fits.

2.3 Creating composite spectra

Most of the individual 1D spectra in our sample do not have sufficient S/N to be able to conduct a detailed spectroscopic characterization. We therefore created composite spectra of various subsamples of galaxies for a detailed analysis. We masked out sky lines in the individual observed frame spectra located at 5577, 5592 and 6302 Å. The spectra were then shifted into the rest-frame using the systemic redshifts derived from a double Gaussian fit to the [O II] line as described in Section 2.2. We defined a continuum using a ninth-order polynomial fit in seven wavelength windows in which we do not expect any emission or absorption line features and divided each spectrum by this continuum. All spectra were then normalized to a common median of 1 in the wavelength range of 2650–2750 Å. This window is chosen to be featureless near the absorption lines we are interested in studying. The spectra are then smoothed by a 5 pixel boxcar (1.5 Å) in order to reduce noise in the spectra, before co-adding.

The composite spectra are clipped averages of all the individual spectra making up the stack where the clipping procedure is such that 10 per cent of the lowest and highest points contributing at each pixel are rejected from the stack leading to a total of 20 per cent of the pixels being rejected. As can be seen later, this procedure can also remove some signal from the composite spectra but due to the presence of significant noise in many of the composites, such a clipping is essential in order to ensure reliable line detections. Errors on these composites are determined from jackknife sampling the individual spectra making up the stack.

2.4 Galaxy properties

Our spectroscopic survey was conducted in well-studied fields meaning that our galaxies have ancillary photometric data from optical to radio wavelengths. These data can be used to derive a range of physical properties such as the star formation rates, bolometric luminosities, dust temperatures and crude stellar masses of the galaxies.

2.4.1 Star formation rates and dust temperatures

The star formation rates are calculated from the $S_{1.4\,\rm GHz}$ radio fluxes as the [O II] luminosity is highly dependent on both the metallicity and extinction and therefore not a good proxy for unobscured star-formation. We use the latest *Herschel* radio–FIR (far-infrared) correlation of $q = 2.4 \pm 0.24$ (Ivison et al. 2010) to calculate the 8–1000 μm infrared luminosities from the radio fluxes after k-correcting the radio flux assuming a spectrum with $S_\nu \propto \nu^{-0.8}$. The star formation rate is then calculated using the relation from Kennicutt (1998):

$$\mathrm{SFR}({\rm M}_{\odot}\,{\rm yr}^{-1}) = 4.55 \times 10^{-44} L_{\rm IR}\ ({\rm erg\,s^{-1}\,cm^{-2}\,Hz^{-1}}). \quad (1)$$

In galaxies with strong AGN signatures, there will also be some contribution to the radio flux from the AGN, so the star formation rates should be taken as upper limits. Both the total infrared luminosity and the star formation rates derived for all galaxies are presented in Table 3.

Table 2. Summary of DEIMOS sample of SMGs (top) and SFRGs (bottom).

Source	RA	Dec.	z	$S_{1.4}$ (μJy)	S_{850} (mJy)	R_{AB}	σ([O II]) (km s^{-1})[a]	12+log(O/H)	Class
					SMGs				
sxdf28a	02:18:06.92	−04:59:12.7	1.114	94 ± 16	$4.8 \pm ^{2.2}_{2.7}$	22.54	190 ± 30	>8.7	AGN[b]
sxdf47a	02:17:34.36	−04:58:57.2	1.180	166 ± 14	$3.0 \pm ^{1.6}_{1.9}$	24.85	120 ± 20	8.1 ± 0.2	SB
sxdf47b	02:17:34.40	−04:58:59.8	1.178	55 ± 14	$3.0 \pm ^{1.6}_{1.9}$	23.02	160 ± 10	>8.9	SB
sxdf55	02:17:51.87	−05:04:47.0	1.628[c]	42 ± 14	$3.9 \pm ^{2.2}_{2.7}$	–	–	–	SB
sxdf05	02:18:02.86	−05:00:30.9	1.087	526 ± 14	$8.4 \pm ^{1.7}_{1.9}$	24.50	380 ± 30[d]	>8.7	AGN
sxdf35	02:18:00.87	−04:53:05.7	1.254	66 ± 15	$5.3 \pm ^{1.8}_{2.1}$	22.93	200 ± 20	>7.9	AGN
sxdf28c	02:18:06.42	−04:59:20.1	1.627	74 ± 20	$4.8 \pm ^{2.2}_{2.7}$	–	60 ± 10	>8.2	AGN[e]
sxdf12	02:17:59.29	−05:05:04.0	1.627	39 ± 16	$5.7 \pm ^{1.7}_{1.8}$	24.03	90 ± 40	>8.4	SB
sxdf47c	02:17:33.62	−04:58:58.2	1.405	64 ± 13	$3.0 \pm ^{1.6}_{1.9}$	23.85	140 ± 30	–	AGN
sxdf88	02:18:01.49	−05:04:43.7	1.518	40 ± 10	$4.5 \pm ^{2.1}_{2.5}$	24.80	250 ± 10[d]	–	SB
gn30	12:36:52.75	+62:13:54.6	1.359	29 ± 8	1.8 ± 0.5	22.7[e]	120 ± 5	8.2 ± 0.1	SB
gn34	12:37:06.22	+62:21:11.6	1.363	22 ± 5	5.6 ± 1.6	22.9[e]	90 ± 10	> 9.0	SB
lock76	10:51:49.18	+57:28:40.7	0.711	44 ± 9	$4.7 \pm ^{2.5}_{3.1}$	21.03	100 ± 20	6.7 ± 0.1	AGN/e(a)
lock77	10:51:57.14	+57:22:10.1	1.464[c]	16 ± 4	$3.2 \pm ^{1.2}_{1.3}$	26.50	–	–	SB
lock73	10:51:42.16	+57:22:18.1	1.423	31 ± 9	$3.5 \pm ^{1.9}_{2.3}$	23.63	80 ± 10	>8.7	SB
lock24	10:52:00.53	+57:20:40.5	1.415	27 ± 7	2.7 ± 1.2	23.74	–	>8.1	SB
lock40	10:52:01.87	+57:19:18.4	1.761	33 ± 13	$3.0 \pm ^{1.1}_{1.2}$	25.95	–	–	SB
lock87	10:51:53.45	+57:17:30.4	1.660[c]	85 ± 5	$3.4 \pm ^{1.5}_{1.7}$	25.58	–	–	SB
lock38	10:53:07.19	+57:24:31.4	1.523	56 ± 7	6.5 ± 1.9	23.63	120 ± 10	–	SB
					SFRGs				
sxdf1293	02:18:26.74	−04:57:39.9	1.356	31 ± 8	−0.9 ± 2.0	24.74	210 ± 20	>8.8	SB
sxdf490	02:17:31.26	−04:59:23.3	1.583	30 ± 15	−1.3 ± 1.7	24.26	110 ± 10	–	SB
sxdf643	02:17:41.56	−04:54:11.5	1.274	137 ± 14	0.4 ± 1.9	23.56	90 ± 20	7.6 ± 0.2	AGN
sxdf755	02:17:49.96	−04:53:47.6	1.279	108 ± 15	−0.1 ± 1.8	21.88	120 ± 20	7.63 ± 0.08	AGN
sxdf639	02:17:41.35	−04:56:34.6	1.341	67 ± 26	1.3 ± 1.8	23.75	160 ± 20	>8.6	SB
sxdf1204	02:18:19.02	−05:07:02.1	0.989	68 ± 20	0.4 ± 1.9	23.93	130 ± 20	>8.7	SB
sxdf844	02:17:55.27	−05:04:33.8	0.929	123 ± 15	−1.9 ± 2.0	23.42	100 ± 10	6.8 ± 0.2	AGN
sxdf965	02:18:03.67	−04:59:30.5	1.264	128 ± 16	1.3 ± 2.1	23.63	190 ± 20	7.66 ± 0.07	AGN
sxdf704	02:17:46.29	−04:54:39.5	1.456[c]	63 ± 14	2.0 ± 1.9	24.86	–	–	SB
sxdf1219	02:18:20.76	−05:01:17.6	1.095	115 ± 25	1.1 ± 1.9	22.45	140 ± 20	7.3 ± 0.1	AGN/e(a)
sxdf1300	02:18:27.35	−05:00:55.9	1.356	148 ± 21	1.3 ± 1.8	21.30	130 ± 20	>8.9	SB
sxdf966	02:18:03.69	−04:56:04.6	1.291	35 ± 14	0.2 ± 1.7	25.05	190 ± 60	>8.8	SB
lock332	10:51:37.14	+57:29:41.8	1.143	720 ± 12[f]	−1.3 ± 1.4	22.46	100 ± 10	>8.6	AGN
lock517	10:51:47.13	+57:18:42.0	1.104	59 ± 7	1.5 ± 1.9	22.79	110 ± 10	8.0 ± 0.2	AGN/e(a)
lock218	10:51:50.59	+57:27:51.1	1.341	25 ± 7	−0.4 ± 1.5	25.76	120 ± 50	7.5 ± 0.2	AGN
lock492	10:51:57.86	+57:19:40.2	1.377	30 ± 11	0.5 ± 1.8	23.52	240 ± 10[d]	>9.0	AGN
lock493	10:52:00.42	+57:18:06.3	1.139	32 ± 7	1.1 ± 1.7	23.14	170 ± 5	7.77 ± 0.03	AGN
c03.1420	03:02:36.28	+00:10:57.2	1.318	40 ± 18	1.18 ± 0.99	23.12[g]	130 ± 50	>8.7	SB
c03.14	03:02:29.75	+00:08:42.7	0.857	102 ± 11	0.82 ± 1.05	21.37[g]	130 ± 10	>9.0	AGN[b]/e(a)
c03.56	03:02:49.89	+00:08:27.0	1.320	70 ± 24	−0.63 ± 1.09	23.02[g]	90 ± 10	>9.0	SB
c03.62	03:02:45.99	+00:08:40.9	1.497	42 ± 17	1.13 ± 1.22	23.22[g]	330 ± 30[c]	>8.8	SB

[a]Best-fitting linewidth including the instrumental profile; [b]AGN classification based on 8-μm excess only; [c][O II] line detected at $\leq 2\sigma$; [d]broad [O II] due to proximity to sky line residuals (sxdf05, sxdf88 and c03.62) or multiple components in 2D spectrum (lock492); [e]i_{775W} AB magnitude from Pope et al. (2006); [f]one lobe of compact FR II; [g]I_{AB} magnitude as R-band image in this field suffers from poor background variability. Typical $R - I$ is expected to be 0.4 ± 0.3.

We also calculate the dust temperatures for our SMGs using the empirical relation derived by C05:

$$T_d = \frac{6.25(1+z)}{(S_{850}/S_{1.4})^{0.26}}. \quad (2)$$

These are plotted as a function of the infrared luminosity in Fig. 1 and compared to the higher redshift SMGs from C05. As can be seen, the lower luminosity SMGs also have cooler dust temperatures on account of their 850-μm selection which precludes detection of galaxies with hotter dust temperatures (Chapman et al. 2010; Magnelli et al. 2010).

2.4.2 *Stellar masses*

We derive stellar masses and corresponding errors for all our SMGs and SFRGs using the HYPERZMASS code (Bolzonella, private communication) which is based on the spectral energy distribution (SED) fitting code for photometric redshift determination, HYPERZ

Table 3. Derived properties for DEIMOS sample of SMGs (top) and SFRGs (bottom).

Source	SFR/$M_\odot$ yr^{-1}	$(L_{IR}/L_\odot) \times 10^{12}$	$\log_{10}(M_*/M_\odot)$	A_v	$\log_{10}(M_{dyn}/M_\odot)$
		SMGs			
sxdf28a	170 ± 30	0.95 ± 0.16	11.15 ± 0.01	4.4	10.88 ± 0.34
sxdf47a	340 ± 30	1.95 ± 0.16	10.89 ± 0.01	0.8	10.41 ± 0.34
sxdf47b	110 ± 30	0.64 ± 0.16	$10.37 \pm {}^{0.10}_{0.03}$	2.4	10.70 ± 0.34
sxdf55	200 ± 70	1.14 ± 0.38	–	–	–
sxdf05	870 ± 20	4.98 ± 0.13	$10.28 \pm {}^{0.04}_{0.01}$	3.8	11.48 ± 0.34
sxdf35	160 ± 40	0.91 ± 0.20	10.50 ± 0.01	3.2	10.92 ± 0.34
sxdf28c	350 ± 90	2.02 ± 0.54	$11.26 \pm {}^{0.43}_{0.23}$	5.4	9.52 ± 0.34
sxdf12	190 ± 80	1.07 ± 0.45	$10.43 \pm {}^{0.03}_{0.02}$	3.4	10.17 ± 0.37
sxdf47c	210 ± 40	1.19 ± 0.24	$10.70 \pm {}^{0.03}_{0.35}$	1.8	10.58 ± 0.34
sxdf88	160 ± 40	0.93 ± 0.21	11.19 ± 0.01	4.8	11.10 ± 0.34
gn30	80 ± 20	0.49 ± 0.14	$9.58 \pm {}^{0.22}_{0.02}$	1.4	10.43 ± 0.34
gn34	70 ± 15	0.38 ± 0.09	9.72 ± 0.01	1.8	10.06 ± 0.34
lock76	20 ± 5	0.14 ± 0.03	10.76 ± 0.02	0.6	10.17 ± 0.34
lock77	60 ± 10	0.33 ± 0.08	$10.05 \pm {}^{0.02}_{0.15}$	1.2	–
lock73	105 ± 30	0.60 ± 0.18	9.59 ± 0.01	2.2	9.96 ± 0.34
lock24	90 ± 20	0.51 ± 0.13	$10.67 \pm {}^{0.06}_{0.12}$	2.2	–
lock40	190 ± 80	1.10 ± 0.44	$10.82 \pm {}^{0.01}_{0.09}$	0.8	–
lock87	430 ± 30	2.45 ± 0.14	10.25 ± 0.07	3.0	–
lock38	230 ± 30	1.29 ± 0.15	$10.77 \pm {}^{0.01}_{0.04}$	1.0	10.41 ± 0.34
		SFRGs			
sxdf1293	90 ± 20	0.52 ± 0.14	$10.23 \pm {}^{0.12}_{0.02}$	4.2	11.25 ± 0.34
sxdf490	130 ± 70	0.76 ± 0.39	10.52 ± 0.06	2.2	10.65 ± 0.34
sxdf643	340 ± 40	1.97 ± 0.20	10.22 ± 0.01	3.2	10.36 ± 0.34
sxdf755	270 ± 40	1.57 ± 0.22	10.13 ± 0.01	3.6	10.71 ± 0.34
sxdf639	190 ± 80	1.10 ± 0.43	$10.51 \pm {}^{0.02}_{0.01}$	2.2	11.01 ± 0.34
sxdf1204	90 ± 30	0.50 ± 0.15	$9.99 \pm {}^{0.14}_{0.01}$	4.0	10.78 ± 0.34
sxdf844	130 ± 20	0.77 ± 0.09	$10.24 \pm {}^{0.12}_{0.05}$	0.4	10.43 ± 0.34
sxdf965	310 ± 40	1.80 ± 0.23	$10.84 \pm {}^{0.01}_{0.04}$	2.4	11.15 ± 0.34
sxdf704	220 ± 50	1.29 ± 0.29	$10.37 \pm {}^{0.01}_{0.07}$	1.6	–
sxdf1219	190 ± 40	1.11 ± 0.24	$10.58 \pm {}^{0.01}_{0.13}$	3.6	10.89 ± 0.34
sxdf1300	440 ± 60	2.50 ± 0.36	11.48 ± 0.01	3.8	10.84 ± 0.34
sxdf966	90 ± 40	0.52 ± 0.21	$9.60 \pm {}^{0.33}_{0.01}$	3.4	11.16 ± 0.35
lock332	1360 ± 20	7.77 ± 0.13	$11.68 \pm {}^{0.03}_{0.23}$	4.8	10.48 ± 0.34
lock517	100 ± 10	0.58 ± 0.07	$11.46 \pm {}^{0.07}_{0.01}$	6.0	10.61 ± 0.34
lock218	70 ± 20	0.41 ± 0.12	$11.45 \pm {}^{0.57}_{1.25}$	2.6	10.75 ± 0.36
lock492	90 ± 30	0.53 ± 0.19	$10.97 \pm {}^{0.35}_{1.18}$	5.2	11.38 ± 0.34
lock493	60 ± 10	0.34 ± 0.07	11.94 ± 0.01	6.0	11.07 ± 0.34
c03.1420	110 ± 50	0.63 ± 0.29	$10.81 \pm {}^{0.11}_{1.04}$	4.8	10.81 ± 0.36
c03.14	90 ± 10	0.52 ± 0.06	$11.11 \pm {}^{0.54}_{0.02}$	5.0	10.79 ± 0.34
c03.56	190 ± 70	1.10 ± 0.38	$10.51 \pm {}^{0.92}_{0.51}$	6.0	10.36 ± 0.34
c03.62	160 ± 60	0.92 ± 0.37	$11.15 \pm {}^{0.40}_{1.04}$	2.2	11.66 ± 0.34

(Bolzonella, Miralles & Pelló 2000). The code is used to fit an SED to the available optical and infrared galaxy photometry in each field including subsets of MUSYC U; Subaru B, R, i, z; *HST*-ACS B, V, i, z; MUSYC J, H, K; and *Spitzer* IRAC 3.6, 4.5, 5.8 and 8.0 μm. The *Spitzer* IRAC photometry for the Lockman and CFRS03 fields came from our own General Observer (GO) programme as well as from publicly available data from various Legacy and Guaranteed Time Observation (GTO) programmes obtained through the *Spitzer Science Center (SSC)* archive, and was reduced and combined using standard SSC pipeline products. Optical and infrared photometry for the Lockman SMGs was taken from the catalogues of Dye et al. (2008). The photometry for SXDF SMGs was obtained from the catalogues in Clements et al. (2008), while that of the SFRGs came from Cirasuolo et al. (2010). The HDF IRAC and *HST*-ACS photometry came from Pope et al. (2006) and Giavalisco et al. (2004). We use a set of nine Bruzual & Charlot (2003) templates with exponentially declining star formation histories with time-scales, τ between 0.1 and 30 Gyr as well as a constant star formation history

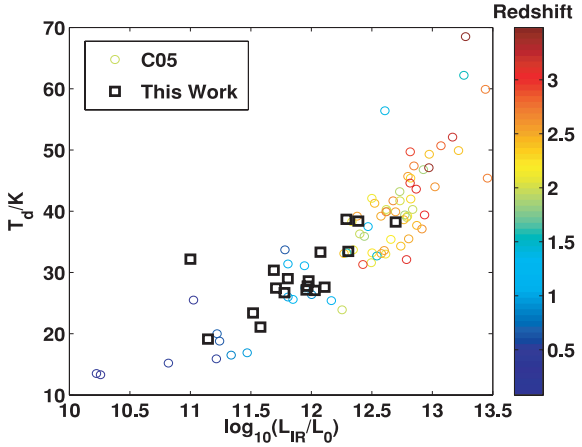

Figure 1. Far-infrared luminosity versus dust temperature for our sample of SMGs compared to the higher redshift SMGs from C05. The C05 sample has been colour-coded according to redshift. It can be seen that the 850-μm selection of these sources results in an apparent trend of dust temperature with infrared luminosity where lower luminosity galaxies are seen to have cooler dust temperatures.

template. All the templates assume a Chabrier (2003) initial mass function (IMF) and are at solar metallicity and we fit extinction values between $A_v = 0$ and 6.0.

The mass-to-light ratios in the *H* band as well as the dust extinction are derived from the best SED fits, and the errors quoted represent the 68 per cent lower and upper confidence limits obtained from the full probability distribution associated with the best chi-squared fit. These errors are very large (of the order of 1 dex) in some cases where a poor fit to the photometry was obtained. The derived stellar masses and dust extinctions for our sample can be found in Table 3. We caution however that most of our galaxies are highly obscured systems with large degeneracies among age, reddening and star formation histories. The actual errors in the stellar masses due to uncertainties in template-fitting and dust extinction are probably therefore considerable. Wardlow et al. (2011) for example find stellar masses that are 5× lower than those estimated by Dye et al. (2008) for SMGs due to difficulties in disentangling the underlying old stellar population in SMGs from the recent burst even when correcting to the same IMF.

The median stellar mass for SMGs in our sample is $(3 \pm 0.2) \times 10^{10}\,M_\odot$ and for SFRGs $(6 \pm 0.8) \times 10^{10}\,M_\odot$. If we had instead adopted a constant mass-to-light ratio in the *H* band of 5.6 (Hainline et al. 2011), this would lead to median stellar masses of $(4 \pm 0.2) \times 10^{10}\,M_\odot$ and $(2 \pm 0.2) \times 10^{10}\,M_\odot$ for SMGs and SFRGs, respectively. The quoted uncertainties reflect the variance in the sample average. For comparison to these values, Wardlow et al. (2011) measure a median stellar mass of $(9 \pm 1) \times 10^{10}\,M_\odot$ for SMGs with photometric redshift ∼2.2 while Hainline et al. (2011) find a stellar mass of $(7 \pm 1) \times 10^{10}\,M_\odot$ for a spectroscopic sample at similar redshifts. Unlike in Hainline et al. (2011), however, we have not subtracted any AGN contribution to the continuum at 8 μm for the galaxies in our sample, so our stellar masses for AGN-dominated systems should be interpreted as upper limits. Given the large uncertainties in the mass estimates, we conclude that the stellar masses at $z \sim 1.3$ and 2 are not significantly different. In all subsequent analysis, we use the stellar masses derived from the full SED fits as presented in Table 3.

2.4.3 *Metallicity and AGN content*

A subset of the galaxies in our sample has been classified as AGN-dominated versus starburst-dominated (Alaghband-Zadeh et al., in preparation) based on various factors such as X-ray properties, [Ne V] detection and [Ne III]/[O II] ratio. These authors also derive metallicities by considering [Ne III]/[O II] ratio as a metallicity indicator (Shi, Zhao & Liang 2007). The metallicities and classifications derived by these authors are presented in Table 2 and will be used to divide galaxies into different subsamples later in the paper. We note here, however, that some of our galaxies appear to have very low metallicities derived from the high [Ne III]/[O II] ratio. This high flux ratio could arise from the presence of a strong AGN rather than an intrinsically low metallicity galaxy (Nagao, Murayama & Taniguchi 2001) and the former is more likely as SMGs and SFRGs are seen to be very massive systems (Section 2.4.2) which are likely to already have been enriched to solar metallicities (Swinbank et al. 2004).

3 ANALYSIS AND RESULTS

3.1 Redshift and luminosity distribution

The sample of SMGs and SFRGs with secure redshifts that are analysed in this study has been summarized in Tables 2 and 3. In Fig. 2 we show the redshift distribution for SMGs and SFRGs in our sample compared to the higher redshift SMGs (C05) and SFRGs (C04) observed with LRIS. The SMG distribution has been scaled by the total area of each survey – 721 arcmin^2 in C05 and 278 arcmin^2 in this study. The SFRG distribution was not scaled as the SFRGs were chosen as mask fillers making it difficult to assess their total survey area and completeness. As such, they are over-represented in this study while being under-represented in C04 relative to C05. It can clearly be seen that this spectroscopic sample of SMGs and SFRGs helps us to effectively fill in the *redshift desert* at $z \sim 1.5$.

In Fig. 3, we also show the redshift versus bolometric luminosity distribution for our galaxies compared to those of C04 and C05. Both this sample and the C04 and C05 samples have been selected in the same manner using their 850-μm fluxes and radio data. As can be seen in Fig. 3, selecting sources at a constant radio flux allows us to probe lower luminosity populations at lower redshifts. However, the 850-μm fluxes of SMGs at $z \sim 1.5$ and 2 should be reasonably similar due to the effects of the negative *k*-correction at sub-mm wavelengths. As the SMGs in both this work and C05 were selected based on both their radio and 850-μm fluxes, the differences in luminosity between the two populations likely arise due to a combination of the radio *k*-correction and some intrinsic luminosity evolution.

3.2 [O II] linewidths and dynamical masses

While the S/N in the majority of our spectra is not good enough to be able to detect many interstellar absorption features, the [O II] emission line is detected at high significance in almost all the spectra and is the main line used for redshift measurement. In this section, we characterize the [O II] linewidth in the galaxies in our sample and use these to derive circular velocities and dynamical masses. The σ-values obtained from fitting two Gaussians of equal width to the [O II] doublet are tabulated in Table 2. There were a few sources for which the [O II] fit was poor as a result of the line being close to the edge of the spectrum or close to sky line residuals. While crude redshifts were still derived for these galaxies,

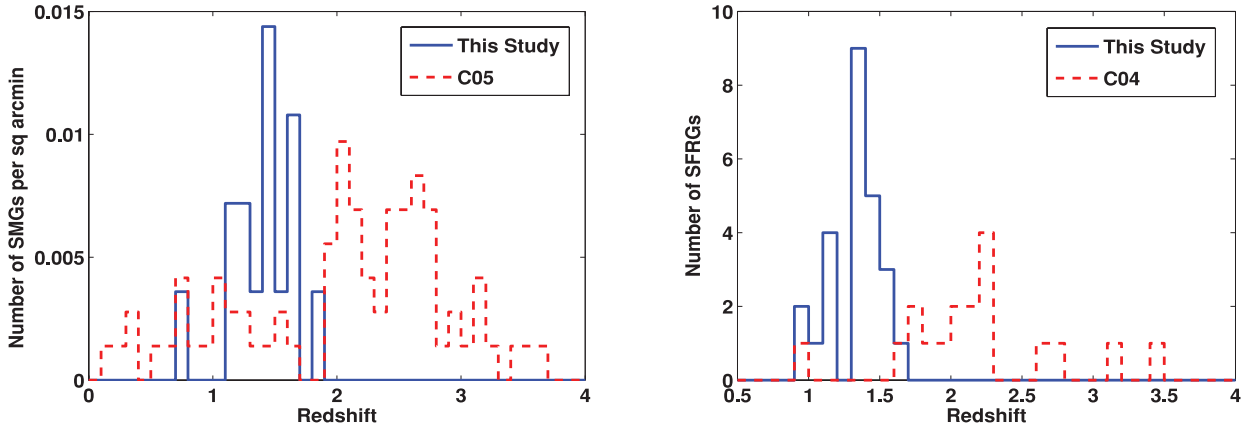

Figure 2. Redshift distribution of SMGs per unit area (left) and SFRGs (right) for our sample compared to the SMGs and SFRGs studied by C05 and C04, respectively. The SFRG distribution is not scaled by total area as the SFRGs were selected as mask fillers making it difficult to assess their total survey area and completeness. It can be seen that our sample helps fill in the redshift desert between redshifts of 1.2 and 1.7 in previous studies.

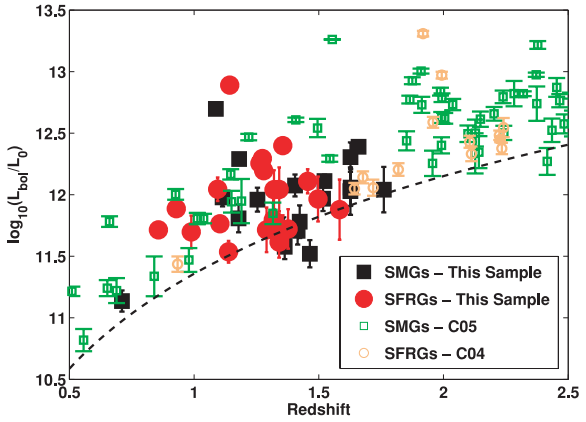

Figure 3. Redshift versus total infrared luminosity for our sample of SMGs and SFRGs compared to the SMGs and SFRGs studied by C04 and C05 (light symbols). The black dashed line shows the variation in infrared luminosity with redshift for a radio source with $S_{1.4\,\mathrm{GHz}} = 30$ μJy. It can be seen that selecting sources at a constant radio flux allows us to probe lower luminosity populations at lower redshifts.

the σ-measurement was highly uncertain and therefore not quoted. These galaxies have been flagged in Table 2. In addition, a few galaxies show very broad [O II] emission. In most cases, this is due to the proximity to night sky lines although one galaxy – lock492 – does show some evidence for multiple components in the [O II] emission seen in the 2D spectrum. Again, these galaxies have been flagged in Table 2.

In order to derive circular velocities and dynamical masses for the galaxies, the line is corrected for an instrumental broadening of 120 km s^{-1}. We calculate the dynamical mass:

$$M_{\mathrm{dyn}} = \frac{C v_{\mathrm{c}}^2 R}{G}, \tag{3}$$

where R is the radius, G is the gravitational constant and C is a constant that depends on the galaxy's mass distribution, velocity field and inclination. C is assumed to be 2.1 for a rotating disc (Neri et al. 2003) assuming an inclination correction of $\sin(i) = 0.5$ (Carilli & Wang 2006), and $C = 5$ for an isotropic virialized system. We compute dynamical masses for both the isotropic and rotating disc estimators and take the true dynamical mass of the galaxy to be the average of these two estimators. For the radius, we assume $R =$ 6 kpc consistent with that found from Hα observations of SMGs (Swinbank et al. 2004) and with the typical size of the [O II] emission region in our 2D spectra. The dynamical masses are presented in Table 3. The mean dynamical mass is $(3.0 \pm 0.3) \times 10^{10}$ M$_\odot$ for SMGs and $(5.9 \pm 0.3) \times 10^{10}$ M$_\odot$ for SFRGs which is consistent with the higher redshift sample of SMGs studied by Swinbank et al. (2004) after taking into account differences in assumptions about the constant, C. The error bars on these mean estimates represent the sample variance but there are also significant systematic uncertainties in the computation of these dynamical masses in particular arising from assumptions about the mass distribution in the galaxies as well as their inclination on the sky. The virial mass estimate detailed above necessarily assumes that [O II] emission follows the total mass distribution of the galaxies. Nebular regions in galaxies are often centrally concentrated, so this assumption will almost certainly lead to an underestimate of the total dynamical mass. In addition, tidal tails from mergers may result in an additional contribution to the dynamical mass from the moment of inertia of the system although the departure from virial is likely to be small in early merger stages. Genzel et al. (2003) find that mergers may lead to a factor of 2 increase in the dynamical mass estimates, likely driven by differences in assumptions regarding the value of R for mergers.

In order to aid our comparison of the dynamical and stellar masses, we consider the typical sizes of the regions from which the nebular and stellar emissions originate. The [O II] region has already been seen to extend to ∼6 kpc. *HST* studies of $z \sim 2$ SMGs suggest typical half-light radii of 2.8 ± 0.4 kpc in the H band (Swinbank et al. 2010). Targett et al. (2011) measure a slightly larger value of 3.4 ± 0.3 kpc in the K band from ground-based imaging. These near-infrared bands are typically used to calculate the mass-to-light ratio for the stellar mass estimates, so we can see that the effective stellar mass aperture is around a factor of 2 smaller than the kinematic aperture assumed in the dynamical mass estimates.

In Fig. 4 we present the stellar mass versus dynamical mass plots for all our galaxies. The average dynamical masses are similar to the average stellar masses of SMGs and SFRGs computed in Section 2.4.2 and mostly consistent within the large systematic uncertainties in both mass estimates which we estimate to be of the order of 1 dex. Several of the AGNs have their stellar masses overestimated due to excess emission at 8 μm.

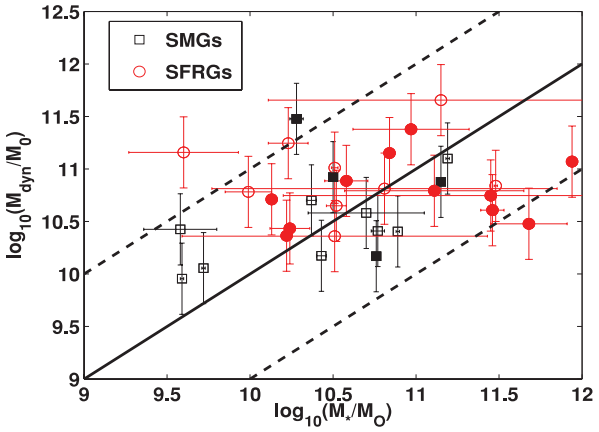

Figure 4. Stellar versus dynamical mass for our sample of SMGs and SFRGs. Galaxies with AGN signatures are shown using filled symbols. The solid line indicates equal masses while the dashed lines represent systematic uncertainties of 1.0 dex due to uncertainties in the mass model in the case of the dynamical masses and uncertainties in the SED fits in the case of the stellar masses.

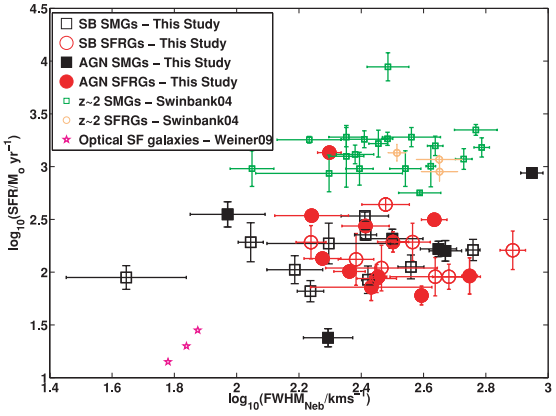

Figure 5. Nebular linewidths for our sample of SMGs and SFRGs versus their star formation rate derived from the infrared luminosity compared with $z \sim 2$ SMGs and SFRGs from Swinbank et al. (2004) and optically selected star-forming galaxies from Weiner et al. (2009). The filled symbols denote AGNs. We see that our sample of galaxies has comparable nebular linewidths and therefore dynamical masses to $z \sim 2$ SMGs and SFRGs but their star formation rates are considerably smaller than those in the $z \sim 2$ SMGs and SFRGs. By contrast, both the star formation rates and nebular linewidths are significantly larger than those in optically selected star-forming galaxies at similar redshifts (Weiner et al. 2009).

In Fig. 5, we plot the [O II] full width at half-maximum as a function of the star formation rate derived from the infrared luminosities. For reference, we also plot the Hα linewidths for the higher redshift sample of SMGs from Swinbank et al. (2004) as well as the [O II] linewidths and star formation rates for optically selected star-forming galaxies at $z \sim 1.5$ (Weiner et al. 2009). There is a large scatter in the nebular linewidths for both samples of SMGs/SFRGs but they overlap, suggesting that many SMGs and SFRGs at redshift 1.3 have dynamical masses similar to those at redshift 2. We conclude that while SMG bursts are occurring in haloes of similar masses at $z \sim 1.3$ and 2.2, the lower redshift SMGs are intrinsically less luminous. In contrast to the SMG/SFRG population, the linewidths for the optically selected sample are considerably smaller suggesting that dust-enshrouded sub-mm galaxies at $z \sim 1.5$ are more massive than optically selected galaxies at the same redshift.

3.3 Composite spectra

Having considered the [O II] line properties of individual galaxies in our sample, we now study the composite spectra in detail in order to characterize various lower S/N features that are difficult to detect in the individual spectra. The composite spectra are created as detailed in Section 2.3. The total composite has a continuum S/N of ~7 at 2700 Å. The mean S/N of the individual spectra is ~1.7 by comparison.

We begin by exploring different spectral features in the average spectra of our SMGs and SFRGs. In Fig. 6 we show the composite spectra of all galaxies. In addition to [O II], there are a number of absorption features associated with Mg II, Fe II and Mg I ions marked at the blue end of the spectrum. These are discussed in more detail in Section 3.4.

As mentioned previously, just under half of the galaxies have been classified as AGN based on their X-ray properties, [Ne III] and [Ne V] emission (Alaghband-Zadeh et al., in preparation). The composite spectrum for these sources is shown in the top panel of Fig. 7. We note, as expected, the presence of [Ne III] emission at 3869 Å as well as weak [Ne V] emission at 3426 Å. The middle panel of Fig. 7 shows a composite spectrum of the starburst-dominated galaxies, which, by contrast, has no detectable [Ne III] emission despite its similar continuum S/N to the AGN composite.

Four galaxies in the sample also show strong Hδ absorption in addition to [O II] emission as well as a 4000-Å break and Ca K&H absorption features. These are lock76, c03.14, lock517 and sxdf1219. These sources are interpreted as extremely dusty starbursts or e(a) galaxies such as those studied by Poggianti & Wu (2000) and the composite spectrum for these is shown in the bottom panel of Fig. 7. Once again [Ne III] emission is seen in this composite as all these galaxies also show evidence for the presence of an AGN. While the presence of [O II] emission in these galaxies suggests that there is significant ongoing star-formation as is the case for the rest of the sample, the large Hδ equivalent widths could arise from significant dust extinction or a large population of older stars created in a massive burst around 500 Myr or so ago. The former explanation is more likely given that these galaxies are currently observed in the ULIRG phase.

We find that the e(a) galaxies are generally brighter and bluer than the rest of the sample. A plausible interpretation is that these systems are seen at a slightly later evolutionary stage on their path to becoming post-starbursts where the stars have had time to diffuse out and the dust has cleared revealing a bluer burst population. We also find that degrading the spectra of the e(a) galaxies to an S/N of 1.7 (typical for the individual spectra in our sample) still allows for detection of the Hδ absorption feature confirming that this feature is only present in a subset of our sample. The numbers in our sample are too small to be able to draw any definite conclusions but likely reveal an interesting subpopulation in SMG/SFRG selection that merits further study.

The galaxy c03.14, one of the four e(a) dusty starbursts, is also the highest S/N spectrum in our sample and the Mg II 2800 doublet is robustly detected in the spectrum as seen in Fig. 8. The average Mg II velocity relative to [O II] is found to be -20 ± 60 km s^{-1} consistent with these features originating at the systemic redshift of the galaxy which has a redshift error of 23 km s^{-1}. We conclude that Mg II here is not associated with any outflowing gas. We have already noted that the rest-UV spectra of e(a) galaxies such as c03.14 are likely to show

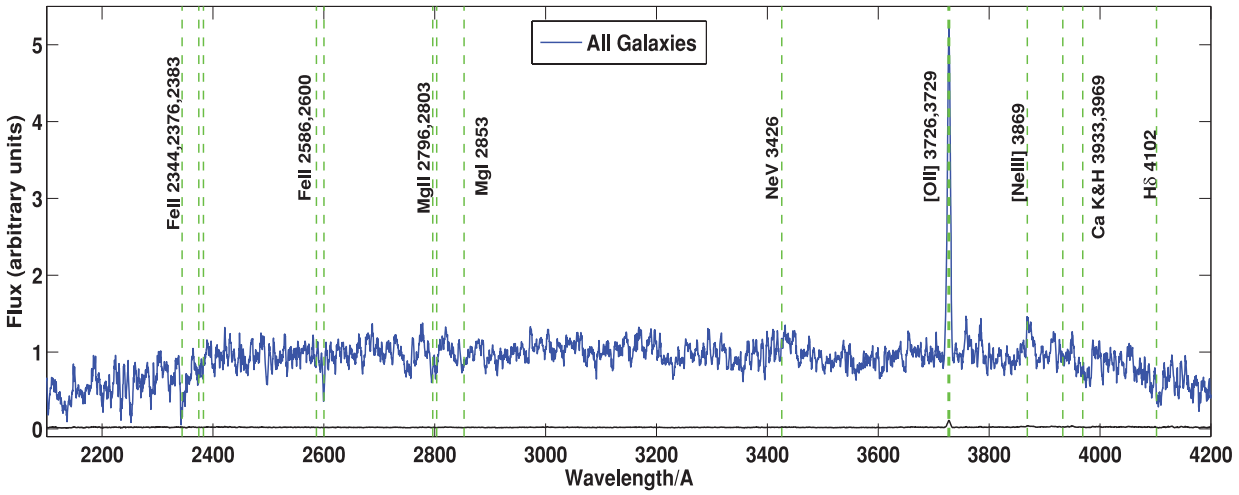

Figure 6. Composite spectrum of all SMGs and SFRGs with robust redshift estimates in our sample in units of F_ν. The line at the bottom of the panel denotes the error spectrum obtained from jackknife sampling the individual spectra making up the composite. As can be seen from the error spectrum, this clipping procedure also removes some signal from the emission lines but is necessary in order to get reliable absorption line identifications.

signatures of both actively star forming regions which suffer from heavy dust extinction, and older more diffuse stellar populations that are less obscured. The latter are predominantly composed of A, F and G stars. The stellar photospheres of these stars typically also show Mg II absorption so the absorption features we are detecting in this galaxy may have a circumstellar origin. However, the equivalent width of Mg II absorption is large (typically $\sim$1.5 Å) hinting at an interstellar rather than circumstellar origin. We discuss this point in more detail in the following section.

3.4 Outflows in composite spectra

The composite spectrum of SMGs and SFRGs at $z \sim 1.3$ (Fig. 6) has numerous absorption features associated with the ISM in these galaxies. These features are now used to look for signatures of outflowing gas in these systems. However, before the absorption lines can be used to measure outflows, we need to convince ourselves that these spectral features are indeed associated with the ISM in the galaxies rather than the stellar photospheres of an old stellar population that is less obscured by dust in the optical/UV than the more recent burst. Interstellar lines can be distinguished from circumstellar lines as they are often seen to be asymmetric and highly saturated. As a consequence, they have large equivalent widths dominated by the velocity dispersion of the gas rather than its column density as is the case for circumstellar absorption (Gonzalez Delgado et al. 1998). Furthermore, Mg II absorption originating in A and F stars is rarely blueshifted relative to systemic. In the rarest and brightest of such stars, the maximum blueshift seen is $\sim -100\,\mathrm{km\,s^{-1}}$ (Snow et al. 1994). In order to remove any contaminating circumstellar absorption, we therefore only measure outflow velocities from pixels at $< -100\,\mathrm{km\,s^{-1}}$ relative to systemic.

We start by excluding the four e(a) galaxies with obvious spectral signatures of >100-Myr-old stellar populations, from our composite spectrum in order to quantify the effect they have on the average velocities of the absorption lines. The galaxies for which the [O II] line fit was noisy making the systemic redshift estimates more uncertain as well as those where the [O II] line was very broad due to proximity to night-sky residuals or the presence of multiple components, are excluded from the stack and have been flagged in Table 2. This leaves us with a total of 26 SMGs and SFRGs for our composite.

In Fig. 9, we show a zoom-in around the absorption features for the composite spectrum of this sample of 26 galaxies in two windows around 2600 and 2800 Å. The interstellar absorption lines are seen to have asymmetric tails that are blueshifted in velocity relative to the systemic [O II]. We interpret this average blueshift as indicating the presence of outflowing cold interstellar gas in these systems.

Outflow velocities and equivalent widths are measured using the AOD formalism as described in Section 2.2, over a velocity window between -500 and $-100\,\mathrm{km\,s^{-1}}$ for all Mg II and Fe II lines seen in the composite spectrum. While there could in principle still be a contribution to these pixels from the blue wing of a systemic component, this contribution is expected to be small at $v < -100\,\mathrm{km\,s^{-1}}$. The S/N in our composite spectrum is not sufficient to be able to subtract this systemic component from the line profiles. Any pixels that lie above the continuum are discarded in order to exclude any strong emission from the line profiles. The limiting S/N, however, does not allow us to effectively remove any weak emission that may be superimposed on an absorption line wing. The velocities and equivalent widths for Mg II and Fe II derived from our composite spectrum of 26 SMGs and SFRGs are presented in Table 4. The velocities are the mean and rms values derived by looking at the distribution in velocities of all detected lines of a particular ion. The errors on the equivalent widths are obtained from jackknife sampling of the spectra.

We have run a number of tests to check for systematic errors in our velocity and equivalent-width determinations due to noise in the spectra. We find that applying the AOD method to randomly chosen windows in the continuum around the various absorption features results in apparent absorption features being detected with equivalent widths of between 0.1 and 0.5 Å in the range of -500 to $-100\,\mathrm{km\,s^{-1}}$. We therefore only consider lines with $W_\mathrm{o} > 0.7$ Å as detections and flag lines with $W_\mathrm{o} < 1.0$ Å as marginal detections in Table 4. The velocities and equivalent widths in Table 4 were derived by considering all pixels in the absorption lines in a fixed velocity window. We check that if we instead let the velocity window vary such that all pixels that are between 10 and 90 per cent of the continuum value are used to characterize the line, the

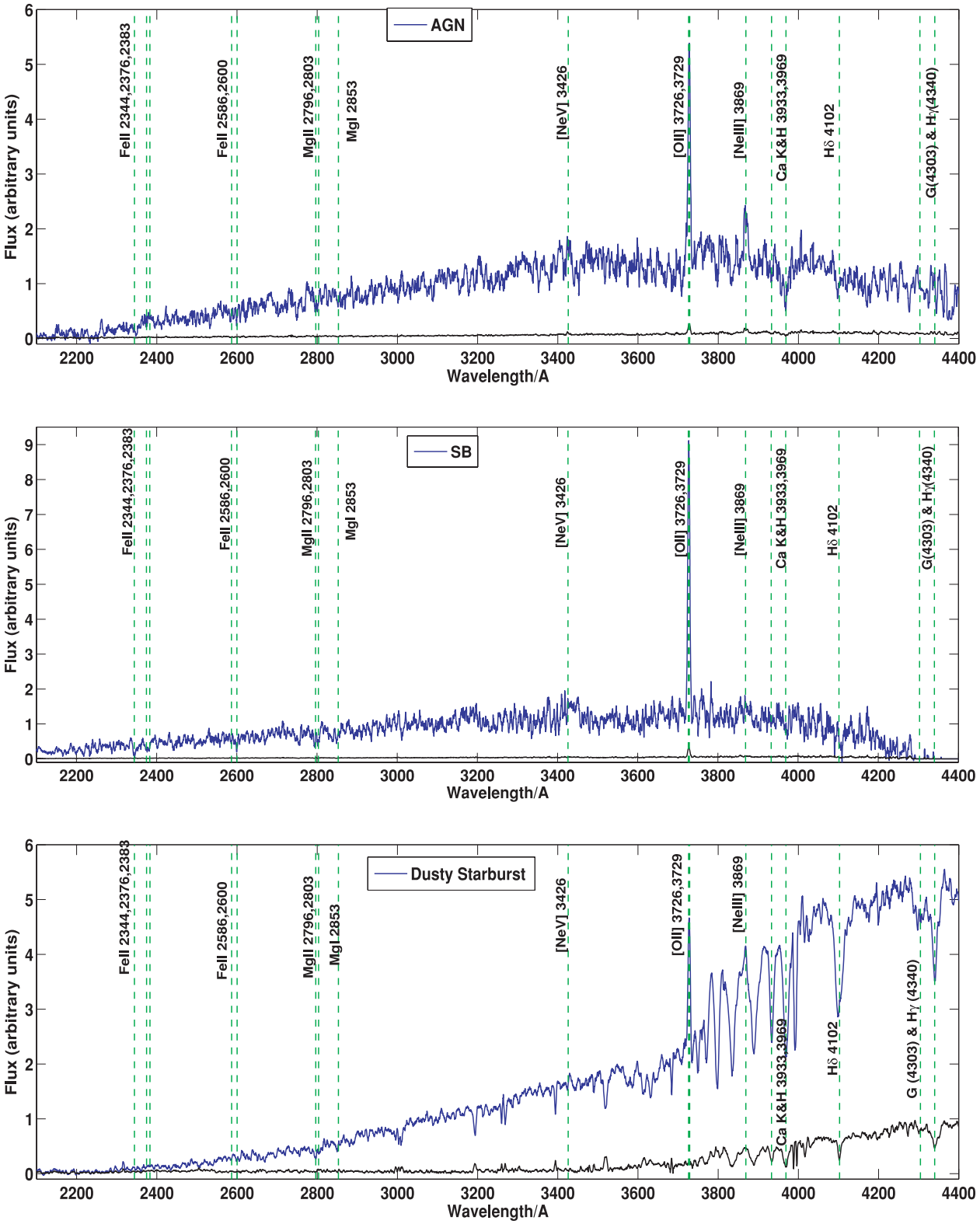

Figure 7. Composite spectra of galaxies showing evidence for AGN activity (top), galaxies dominated by the starburst (middle) and dusty e(a) galaxies (bottom) in the unit of F_ν, illustrating the spectral diversity observed in our SMG/SFRG sample at $z \sim 1.3$. These spectra are shown with the continuum in order to illustrate differences in the continua among the star-forming galaxies, AGNs and the dusty starbursts. The roll-off at the red-end in the AGN and starburst composites is due to the presence of multiple negative sky line residuals at these wavelengths. In each panel, the line at the bottom of the panel denotes the error spectrum obtained from jackknife sampling the individual spectra making up the composite. As can be seen in the error spectra, this clipping procedure also removes some signal, e.g. from weak emission lines such as [Ne v] in the AGN composite.

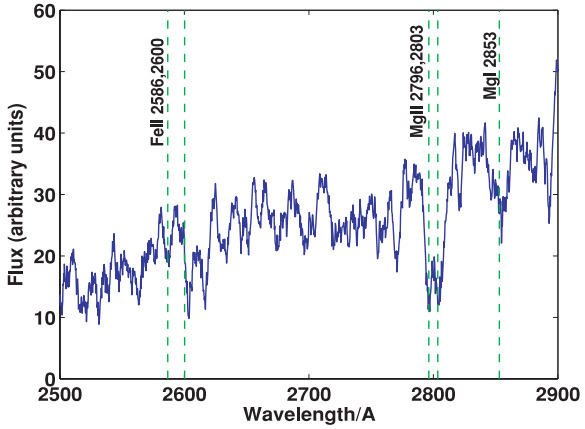

Figure 8. ISM region in the highest S/N spectrum in our sample – c03.14 where the Mg II doublet appears to be at the systemic redshift of the galaxy indicating that it is not associated with outflowing gas in this case.

velocities and widths remain unchanged within the errors. This gives us confidence in the outflow velocity measurements presented despite the significant noise in the continua of the stacked spectra. We also measure terminal velocities from the Mg II 2796 absorption feature by applying the AOD formalism to all pixels in the absorption line profile that are within 90 per cent of the continuum value. These terminal velocities are also presented in Table 4. The errors are very large in some cases where the overall S/N of the composite spectrum is low making it difficult to determine where the line meets the continuum.

For our 26 SMGs and SFRGs excluding the e(a) galaxies, we find a mean Fe II velocity of $-220 \pm 40\,\mathrm{km\,s^{-1}}$ and a mean Mg II velocity of $-260 \pm 50\,\mathrm{km\,s^{-1}}$. Both the Mg II and Fe II ions correspond to the same ionization state and should therefore trace gas with similar physical conditions and therefore velocities. The velocities are consistent with each other as expected and we derive a mean ISM velocity of $-240 \pm 50\,\mathrm{km\,s^{-1}}$. The terminal velocity is around $-500 \pm 100\,\mathrm{km\,s^{-1}}$. Adding the four e(a) galaxies to the composite leaves the velocities and equivalent widths unchanged within the errors.

In Table 4, we also present the equivalent width ratio between Mg II 2796 and 2803 Å. In the case of optically thin absorption, we expect this ratio to be 2. The observed ratio is found to be $1.04 \pm {}^{0.11}_{0.16}$ suggesting that the lines are saturated and the absorption is optically thick. We note that the AOD formalism used to derive line centroids and widths implicitly assumes that the absorption material covers the source completely and homogeneously. For optically thick absorption, the equivalent widths derived from a single parameter fit to the line profiles do not allow us to disentangle the effects of optical depth and covering fraction. This requires multiparameter fits to the absorption line profiles which, due to the limiting S/N of the spectra, is beyond the scope of this work.

Having quantified the average outflow velocity in all SMGs and SFRGs, we now split the galaxies into various subsamples in order to look at the dependence of outflow velocity on galaxy properties. These subsamples are summarized in Table 1 and the velocities and equivalent widths derived from them are given in Table 4. As can be seen in Table 4, there is no significant difference in outflow velocities between SMGs and SFRGs and we therefore treat the two populations as a single uniform sample in the remaining analysis. Similarly, there is no evidence for galaxies classified as AGN driving higher velocity winds. There is also no trend seen between the outflow velocities and the galaxy mass. Fig. 10 illustrates that the Mg II velocities of both our stellar mass subsamples are consistent with those derived by Weiner et al. (2009) for optically selected galaxies at similar redshifts. Given the large systematic uncertainties in both the stellar and dynamical mass estimates of these galaxies (Sections 2.4.2 and 3.2), this lack of correlation is perhaps not surprising.

We do however see some evidence for galaxies with high FIR luminosities (derived from the radio fluxes) as well as those with high [Ne III]/[O II] line ratios powering higher velocity winds. These trends are now explored in more detail.

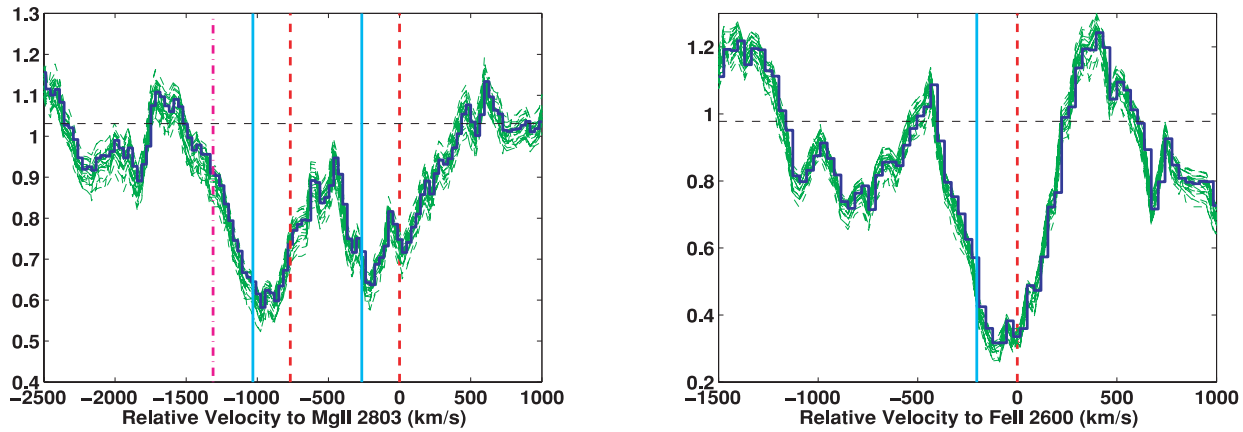

Figure 9. Zoom-in around the Mg II 2800 doublet (left) as well as the Fe II 2600 absorption feature (right) for our composite spectrum of 26 SMGs and SFRGs with reliable [O II] redshifts and excluding the four dusty starbursts. The absorption line regions have been additionally smoothed for presentation purposes. The thick dark line is the composite spectrum while the lighter lines show the errors in the absorption line profile from the different jackknife samples. The dashed vertical lines mark the expected velocities of the various absorption derived from the systemic redshifts of the galaxies. These features include Mg II 2796.35 Å ($-770\,\mathrm{km\,s^{-1}}$ relative to Mg II 2803), Mg II 2803.53 Å ($0\,\mathrm{km\,s^{-1}}$ in the left-hand plot) and Fe II 2600.17 Å ($0\,\mathrm{km\,s^{-1}}$ in the right-hand plot). The solid vertical lines indicate the actual centroid velocities of the lines measured between -500 and $-100\,\mathrm{km\,s^{-1}}$ using the AOD formalism. The dot–dashed vertical line in the left-hand panel shows the terminal velocity of Mg II 2796 measured by applying the AOD formalism to pixels in the absorption line profile that are >90 per cent of the continuum value. No terminal velocity was measured for Fe II 2600 as the blue wing of this line runs into a weaker Mn II absorption feature at 2594.5 Å making it difficult to determine where the line meets the continuum. A definite blueshift is seen in all absorption line velocities relative to systemic indicating the presence of outflowing gas in these galaxies.

Table 4. Mg II and Fe II velocities and equivalent widths for different samples of SMGs and SFRGs. Numbers in brackets are less reliable due to the small equivalent widths of the detected feature and/or blending of features.

Sample	$v^{\rm cen}_{\rm Mg\,II}$ (km s^{-1})	$v^{\rm cen}_{\rm Fe\,II}$ (km s^{-1})	$v^{\rm term}_{\rm Mg\,II}$ (km s^{-1})	$W_{\rm Mg\,II2796}$ (Å)	$W_{\rm Fe\,II2600}$ (Å)	$W_{\rm Mg\,II2796}/W_{\rm Mg\,II2803}$
All [no e(a)]	-255 ± 49	-216 ± 36	$-540 \pm ^{40}_{100}$	$1.48 \pm ^{0.11}_{0.15}$	$1.37 \pm ^{0.16}_{0.15}$	$1.04 \pm ^{0.11}_{0.16}$
All [incl. e(a)]	-258 ± 52	-212 ± 16	$-540 \pm ^{30}_{100}$	$1.09 \pm ^{0.10}_{0.14}$	$1.09 \pm ^{0.13}_{0.11}$	$0.96 \pm ^{0.18}_{0.18}$
SMG	-270 ± 52	-225 ± 35	$-700 \pm ^{40}_{80}$	$2.70 \pm ^{0.34}_{0.18}$	$1.06 \pm ^{0.20}_{0.21}$	$1.97 \pm ^{0.23}_{0.34}$
SFRG	-281 ± 20	-222 ± 39	$-420 \pm ^{120}_{380}$	–	$1.88 \pm ^{0.20}_{0.23}$	–
AGN	-264 ± 20	-246 ± 77	$-580 \pm ^{140}_{40}$	$1.17 \pm ^{0.33}_{0.27}$	–	$0.85 \pm ^{0.29}_{0.43}$
SB	-268 ± 66	-242 ± 48	$-540 \pm ^{70}_{150}$	$2.41 \pm ^{0.30}_{0.18}$	$1.98 \pm ^{0.17}_{0.18}$	$1.43 \pm ^{0.17}_{0.19}$
$L_{\rm IR} > 1.09 \times 10^{12}\,{\rm L}_\odot$	-299 ± 57	-230 ± 44	$-980 \pm ^{230}_{150}$	$1.95 \pm ^{0.30}_{0.26}$	$2.24 \pm ^{0.37}_{0.20}$	$1.07 \pm ^{0.19}_{0.22}$
$L_{\rm IR} < 0.65 \times 10^{12}\,{\rm L}_\odot$	-228 ± 48	-176 ± 20	$-590 \pm ^{160}_{110}$	$1.24 \pm ^{0.45}_{0.40}$	$1.04 \pm ^{0.38}_{0.08}$	$0.68 \pm ^{0.38}_{0.37}$
$12 + \log({\rm O/H}) > 8.4$	-237 ± 61	-216 ± 47	$-330 \pm ^{140}_{120}$	$1.02 \pm ^{0.48}_{0.24}$	$2.10 \pm ^{0.28}_{0.23}$	$0.68 \pm ^{0.53}_{0.25}$
$12 + \log({\rm O/H}) < 8.2^a$	(-303 ± 19)	-272 ± 88	$-810 \pm ^{220}_{270}$	$(1.28 \pm ^{0.34}_{0.26})$	$1.30 \pm ^{0.32}_{0.26}$	$(0.62 \pm ^{0.28}_{0.24})$
$\log_{10}(M_*/{\rm M}_\odot) > 10.80^b$	(-243 ± 27)	-263 ± 43	$(-750 \pm ^{220}_{210})$	$(0.81 \pm ^{0.41}_{0.25})$	$2.40 \pm ^{0.39}_{0.27}$	–
$\log_{10}(M_*/{\rm M}_\odot) < 10.50$	-264 ± 71	-191 ± 32	$-400 \pm ^{20}_{50}$	$1.90 \pm ^{0.21}_{0.26}$	$0.73 \pm ^{0.20}_{0.10}$	$1.53 \pm ^{0.46}_{0.25}$
$\log_{10}(M_{\rm dyn}/{\rm M}_\odot) > 10.50^c$	–	-234 ± 30	$-550 \pm ^{240}_{170}$	–	$2.00 \pm ^{0.17}_{0.15}$	–
$\log_{10}(M_{\rm dyn}/{\rm M}_\odot) < 10.30$	-273 ± 43	-208 ± 29	$-670 \pm ^{80}_{170}$	$2.52 \pm ^{0.19}_{0.20}$	$1.53 \pm ^{0.33}_{0.22}$	$1.47 \pm ^{0.12}_{0.13}$

[a]Mg II 2800 doublet is blended; [b]Mg II 2796 only marginally detected; [c]terminal velocity derived from Fe II 2586.

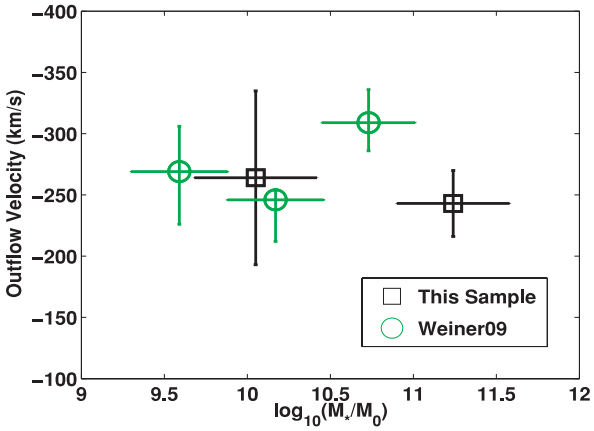

Figure 10. Outflow velocities as a function of stellar mass for our SMGs and SFRGs compared to optically selected star-forming galaxies from Weiner et al. (2009). The luminous radio galaxy velocities are consistent with the optically selected sample.

3.4.1 *Dependence on infrared luminosity*

In order to study the dependence of outflow velocity on infrared luminosity, we split our SMGs and SFRGs into two subsamples with $L_{\rm IR} < 0.68 \times 10^{12}$ and $> 1.09 \times 10^{12}\,{\rm L}_\odot$, so there are roughly equal numbers of galaxies in each sample. The composite spectra are then generated as discussed in Section 2.3. These composites are shown in Appendix A and the derived velocities and equivalent widths are summarized in Table 4.

Various absorption features are detected in both stacks corresponding to transitions of Fe II and Mg II. The average Mg II velocity in the high-$L_{\rm IR}$ stack is found to be $-300 \pm 60\,{\rm km\,s^{-1}}$. The lower $L_{\rm IR}$ composite on the other hand has an average Mg II velocity of $-220 \pm 50\,{\rm km\,s^{-1}}$. We use the Mg II 2796 feature to measure the terminal velocities in both these subsamples by only considering pixels between 90 and 100 per cent of the continuum value in the AOD formalism. This is measured to be $-1000 \pm 200\,{\rm km\,s^{-1}}$ in the high-$L_{\rm IR}$ composite compared to $-600 \pm 200\,{\rm km\,s^{-1}}$ in the low-$L_{\rm IR}$ composite.

A high FIR luminosity implies high star-formation rates assuming the FIR–radio correlation holds. However, this relation also has considerable scatter, for example due to radio-loud AGN which can contribute significantly to the total radio flux even in the absence of significant star-formation. The slight increase in outflow velocity with total FIR luminosity seen in our sample therefore has two possible interpretations. It could signal that galaxies with higher star-formation rates power higher velocity winds as has already been found in local samples (Martin 2005) as well as optically selected galaxies at $z \sim 1.5$ (Weiner et al. 2009). Alternatively, it could provide evidence for a radio-loud AGN powering higher velocity winds as seen in Morganti, Tadhunter & Oosterloo (2005), Alatalo et al. (2011) and Lehnert et al. (2011).

Two of our high-$L_{\rm IR}$ galaxies, lock332 with a radio flux of 720 μJy and sxdf05 with a radio flux of 526 μJy, clearly show evidence for the presence of powerful AGNs. The sub-mm counterpart of lock332 is coincident with one lobe of a compact Fanaroff–Riley type II (FR II) galaxy and both galaxies show strong X-ray emission. The remainder of the high-$L_{\rm IR}$ galaxies however do not show obvious AGN signatures in the radio. We remove the two radio-loud AGNs from our high-$L_{\rm IR}$ composite but find the outflow velocities to remain unchanged within the errors. We therefore conclude that these galaxies do not contribute significantly to the higher outflow velocities in the high-$L_{\rm IR}$ composite and that this signature is therefore primarily dominated by differences in star formation rates between the two subsamples.

The centroid velocities of Mg II for both subsamples are consistent with the Mg II velocities derived by Weiner et al. (2009) for galaxies at the same redshifts with considerably lower star-formation rates. We discuss this trend further and compare to other samples of galaxies in Section 4.2.

Weiner et al. (2009) also find that the equivalent width of Mg II absorption increases with the star formation rate with higher SFR galaxies having equivalent widths that are ∼30 per cent higher than lower SFR galaxies. Having interpreted the high-$L_{\rm IR}$ galaxies as

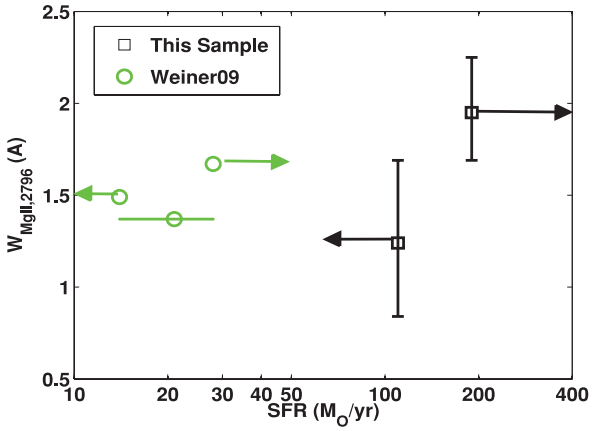

Figure 11. Star formation rate versus equivalent width of Mg II 2796 Å for our sample of luminous radio galaxies as well as optically selected galaxies at similar redshifts from Weiner et al. (2009). The equivalent widths for the two samples are consistent with one another within the errors but show a slight increase at high star-formation rates.

having high star-formation rates, in Fig. 11 we plot the equivalent widths versus star formation rate for both our sample and that of Weiner et al. (2009). Again, our results are consistent with the optically selected galaxies.

3.4.2 Dependence on [Ne III]/[O II] line ratio

Alaghband-Zadeh et al. (in preparation) study the mass–metallicity relation for our sample of galaxies by considering the [Ne III]/[O II] line ratio as a metallicity indicator. However, we have already discussed in Section 2.4.3 how a high flux ratio in these lines could also arise due to the presence of a strong AGN. In this section we divide our sample into two subsets with $12 + \log(\mathrm{O/H}) > 8.4$ and $12 + \log(\mathrm{O/H}) < 8.2$. Due to the ambiguity regarding whether an [Ne III]/[O II] selection is in fact a metallicity cut or simply a different AGN selection to that in Section 2.4.3, we refer to the two subsamples as the *low* [Ne III]/[O II] and *high* [Ne III]/[O II] subsamples.

We show the Mg II doublet in both these subsamples in Fig. 12. Although the line detections are not highly significant given the limiting S/N of the spectra, the Mg II 2800 doublet appears to be separated in the low [Ne III]/[O II] stack while the feature is considerably blended in the high [Ne III]/[O II] stack indicating a range of velocities extending to a tail of $-800 \pm 200\,\mathrm{km\,s^{-1}}$. We conclude that galaxies with high [Ne III]/[O II] line ratios power higher velocity winds. There are two possible interpretations for this. Either galaxies with intrinsically lower metallicities drive faster outflows or the [Ne III]/[O II] line ratio allows us to select the most powerful AGNs which correspondingly propel stronger winds.

The first interpretation is supported by the fact that the terminal velocity in the high [Ne III]/[O II] stack is consistent with the $-700\,\mathrm{km\,s^{-1}}$ terminal velocity measured for the low-metallicity Lyman-break galaxy (LBG) Q2343−BX418 (Erb et al. 2010) with a metallicity of $12+\log(\mathrm{O/H}) = 7.9 \pm 0.2$. The average metallicity derived from [Ne III]/[O II] for the high [Ne III]/[O II] sample is similar – $12+\log(\mathrm{O/H}) = 7.6 \pm 0.5$. However, in the absence of independent metallicity estimates, the current sample does not allow us to identify AGN or metallicity as the main driver for differences in outflow velocities as a function of [Ne III]/[O II].

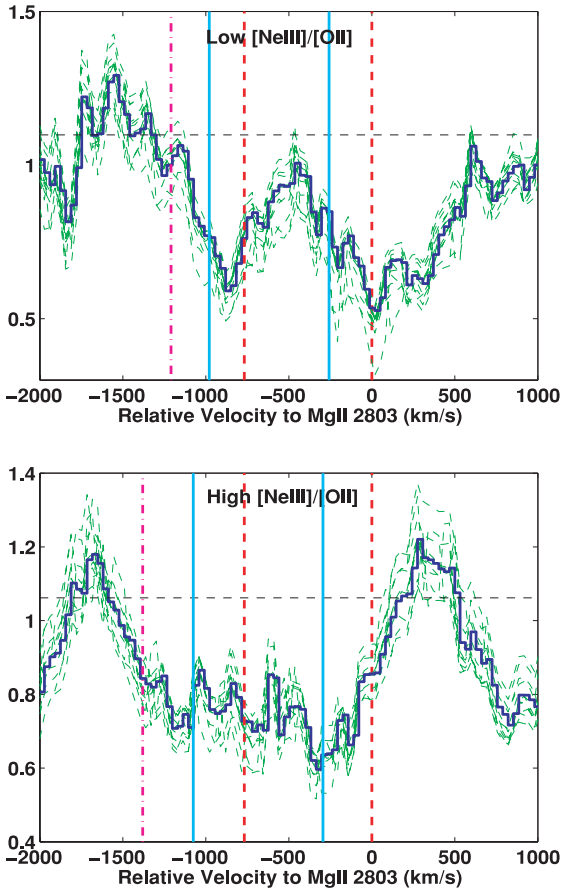

Figure 12. Zoom-in around the Mg II absorption feature for both low [Ne III]/[O II] (top) and high [Ne III]/[O II] (bottom) galaxies. The thick dark line is the composite spectrum while the lighter lines show the errors in the absorption line profile from the different jackknife samples. The dashed vertical lines denote the expected position of Mg II absorption while the solid vertical lines show the actual measured centroid and the dot–dashed vertical line shows the terminal velocity of Mg II 2796. The high [Ne III]/[O II] sample shows a blueshifted tail in Mg II absorption extending to velocities as high as $\sim -800\,\mathrm{km\,s^{-1}}$. This is clearly not seen in the low [Ne III]/[O II] sample suggesting that the wind velocity is correlated with the [Ne III]/[O II] line ratio.

The mean circular velocity of both the high and low [Ne III]/[O II] galaxies in our sample is $80 \pm 30\,\mathrm{km\,s^{-1}}$. The escape velocity is typically ∼3 times the circular velocity for reasonable assumptions about the halo mass distribution (Binney & Tremaine 1987). This implies escape velocities of $\sim 240 \pm 90\,\mathrm{km\,s^{-1}}$ for these galaxies. While the Fe II and Mg II centroid velocities for both low and high [Ne III]/[O II] galaxies are within the 1σ error in this escape velocity, the terminal velocity in the high [Ne III]/[O II] stack is almost a factor of 3 larger than the escape velocity. This suggests that at least some of the gas is able to escape from these galaxies and get into the intergalactic medium.

4 DISCUSSION

4.1 Redshift evolution of SMG/SFRG properties

One of the main aims of our DEIMOS study was to fill in the redshift desert in spectroscopic samples of SMGs and SFRGs at $z = 1.2$–1.7. Previous studies of these populations have typically

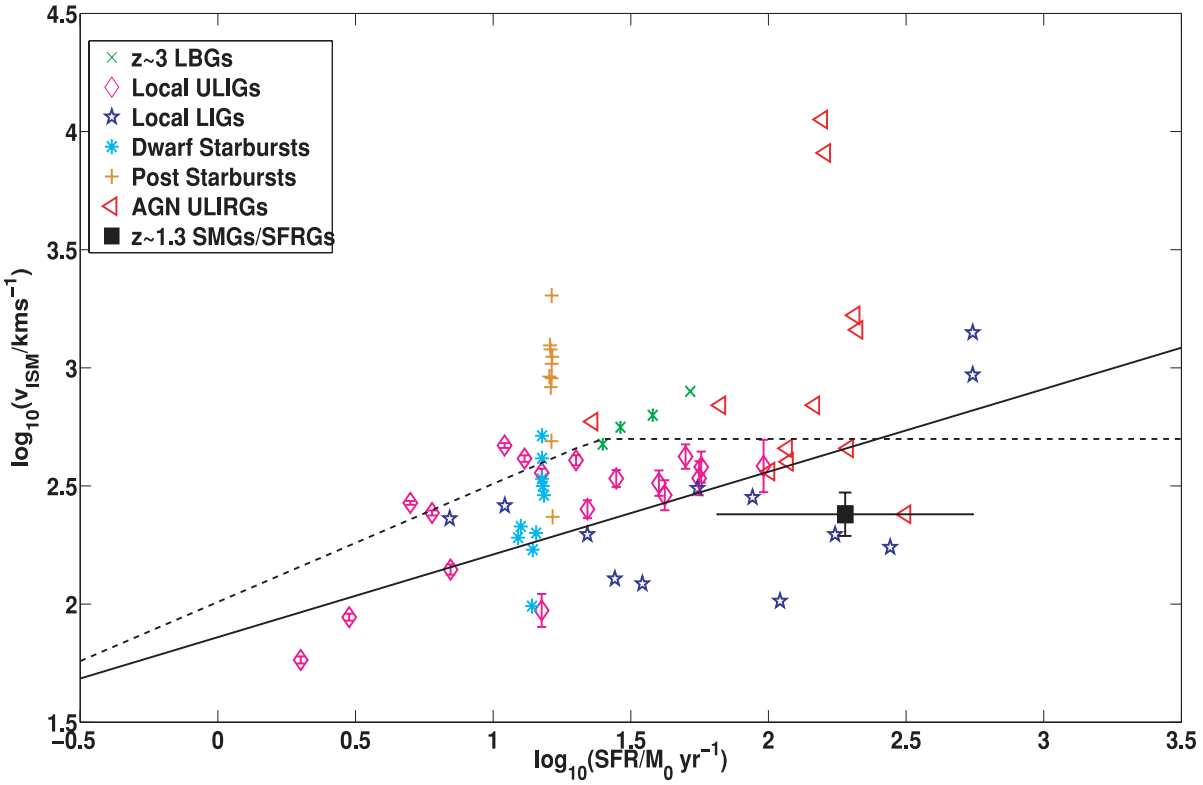

Figure 13. Variation in outflow velocity as a function of the star formation rate for several different samples of galaxies. The solid line shows the local relation from Martin (2005) after correcting for projection effects. The dashed line shows the velocities expected if the cold gas is accelerated by momentum-driven winds to the velocity of the hot gas component taken to be 500 km s^{-1}. Our sample of SMGs and SFRGs is shown as the dark square. The SMG/SFRG average outflow velocity lies within the local envelope and is consistent with the momentum-driven wind model. The average outflow velocity of our redshift 1.3 SMGs and SFRGs is also indistinguishable from those of local LIRGs and ULIRGs.

used blue-optimized spectrographs focused on galaxies at $z \sim 2$ (C05). We have seen that the higher redshift population has higher bolometric luminosities. While this partly arises due to the radio selection of the spectroscopic targets whereby higher redshift sources require higher radio luminosities to be detectable, the additional 850-μm selection of SMG targets is less sensitive to redshift due to the negative k-correction in the sub-mm. Despite their similar 850-μm fluxes, we find that SMGs at $z \sim 1.5$ are an order of magnitude less luminous than at $z \sim 2.2$ suggesting some luminosity evolution in between these redshifts. The clear dearth of SMGs and SFRGs in our sample with $\gtrsim$1000 M$_\odot$ yr^{-1} star formation rates suggests that there is considerable evolution in the star formation rates of these galaxies between redshift 1 and 2 with the peak activity in the population closer to $z \sim 2$. However, the star formation rates at $z \sim 1.3$ are still high enough for these galaxies to be classed as ULIRGs.

In contrast to the strong evolution in the typical star-formation rates of SMGs and SFRGs, we have seen in Section 3.2 that the nebular linewidths and therefore dynamical masses of SMGs and SFRGs at $z \sim 1.3$ are virtually indistinguishable from those at $z \sim 2$. We conclude therefore that the masses of sub-mm galaxies show little evolution between redshifts 1 and 2. However, we find that at $z \sim 1.3$ it appears that most of the baryons in the central regions of these systems are likely to be in the form of stars given the very large stellar masses. This is in contrast to the situation at somewhat higher redshifts where the cold gas component is more significant. Tacconi et al. (2008) for example find a cold-gas fraction in $z \sim 2$ SMGs of up to 50 per cent.

Comparing the star formation rates as well as dynamical masses of our SMG/SFRG population to optically selected star-forming galaxies at similar redshifts clearly demonstrates that we are probing a much more massive, more intrinsically luminous population than the optical samples. Many independent lines of evidence now point to these SMGs and SFRGs being the most likely progenitors of present-day massive elliptical galaxies at $\sim L_{\rm K}^* - 3\,L_{\rm K}^*$ ($M_{\rm K} \leq -24$; Swinbank et al. 2006). Recent studies have shown that such massive ellipticals have stellar masses of $>10^{12}$ M$_\odot$ already assembled by $z \sim 0.7$ (e.g. Banerji et al. 2010), an order of magnitude larger than the typical masses seen in our sample.

4.2 Outflow velocities and star formation rate

Outflow velocities are generally found to scale with the star formation rate such that $V_{\rm wind} \propto {\rm SFR}^{0.3}$. This relationship which has been well determined in the local Universe (Martin 2005) is also found to hold for populations of normal star-forming galaxies at high redshifts (Weiner et al. 2009). Given that the SMGs and SFRGs studied in this work represent some of the most extreme star-forming systems at high redshifts, it is interesting to compare their outflow velocities to those in other systems both in the local Universe and at high redshifts in the context of this $V_{\rm wind}$–SFR relation.

In Section 3.4 we presented some evidence for galaxies with high $L_{\rm IR}$ and those with high [Ne III]/[O II] powering higher velocity winds. However, as can be seen in Table 4, the differences among these various subsamples are significant only at $\sim 2\sigma$ level.

For the purposes of this discussion therefore, we only consider the sample average velocity of $-240 \pm 50\,\mathrm{km\,s^{-1}}$. In Fig. 13, we plot this sample average and compare to various other samples of local as well as high-redshift galaxies covering a large dynamic range in star formation rate of ∼3 dex. These include the LBGs from Shapley et al. (2003); local LIRGs (Heckman et al. 2000) and ULIRGs (Martin 2005); local dwarf starbursts (Schwartz et al. 2006); 'post-starbursts' in the SDSS (Tremonti, Moustakas & Diamond-Stanic 2007); and a sample of AGN-dominated ULIRGs (Rupke, Veilleux & Sanders 2005). In the case of the dwarf starbursts, the star formation rate is crudely estimated from the *B*-band absolute magnitudes quoted in Schwartz et al. (2006). In the case of the local LIRGs, the star formation rate is calculated from the total infrared luminosity from Heckman et al. (2000). Fig. 13 also shows the $V_{\mathrm{wind}} \propto \mathrm{SFR}^{0.3}$ relation as determined by Martin (2005) after correcting for line-of-sight effects, i.e. the fact that face-on discs with bipolar flows will appear to have systematically higher velocities. This line should therefore trace the upper envelope of the V_{wind}–SFR relation assuming there is no evolution in this relation with redshift.

The outflow velocities in our sample are found to be consistent with the local envelope. The median outflow velocities in the local LIRG and ULIRG populations are -330 ± 10 and $-210 \pm 20\,\mathrm{km\,s^{-1}}$, respectively. Within the errors in our outflow velocity measurements, the redshift 1–2 SMGs and SFRGs are therefore indistinguishable in terms of wind velocity from these local galaxy samples. We also note that the median velocities for local LIRGs and ULIRGs are derived from only those galaxies showing evidence for starburst-driven winds. While this is certainly the norm, there are also individual starburst galaxies in the local Universe which do not show blueshifted ISM absorption features. Our outflow velocities, as a consequence of being derived from composite rather than individual spectra, necessarily average over such *no-wind* systems. While these systems would lower the measured equivalent width of the absorption lines, they should not affect the centroid velocities between -100 and $-500\,\mathrm{km\,s^{-1}}$.

In the local Universe, the velocities of cold interstellar gas are found to scale with the star formation rate of the galaxy but the hot-wind traced by X-rays is remarkably uniform in temperature (Martin 1999; Heckman et al. 2000). One hypothesis is that the cool gas in lower luminosity starbursts is not accelerated to the hot-wind velocities as there is not sufficient momentum for this to happen. In a wind model dominated by momentum injection from supernovae or AGNs, the cold gas component traced by the interstellar absorption features is entrained in the hot wind and therefore accelerated to the hot wind velocity. The velocity of the cold gas component, V_{cold}, is given by

$$\frac{V_{\mathrm{cold}}}{V_{\mathrm{hot}}} = \left(\frac{\mathrm{SFR}}{0.24\,\mathrm{M_\odot\,yr^{-1}}}\right)^{0.5} \times \left[\left(\frac{10^{20}\mathrm{cm^{-2}}}{N_H}\right)\left(\frac{200\,\mathrm{pc}}{R_0}\right)\left(\frac{500\,\mathrm{km\,s^{-1}}}{V_{\mathrm{hot}}}\right)\right]^{0.5}, \quad (4)$$

where R_0 is the launch radius, N_H is the column density and V_{hot} is the velocity of the hot wind component (Martin 2005; Murray, Quataert & Thompson 2005). We assume the same upper envelope in the V_{cold}–SFR relation as fitted by Martin (2005) in which $(N_H/10^{22}\,\mathrm{cm^{-2}})(R_0/200\,\mathrm{pc}) \sim 1$. Fig. 13 shows this upper envelope. The hot wind velocity is taken to be a constant $500\,\mathrm{km\,s^{-1}}$ from X-ray measurements (Martin 1999; Heckman et al. 2000). Once the cloud reaches this velocity the ram pressure ceases to accelerate the cold gas any further, resulting in a plateau in the outflow velocities at high star-formation rates.

Our composite spectra do not rule out this plateau. In fact, the outflow velocities in our sample are very similar to those measured in optically selected galaxies at the same redshifts with considerably lower star-formation rates (Weiner et al. 2009). This suggests perhaps that a plateau has already been reached within the parameter space spanned by our $z \sim 1.3$ SMGs and SFRGs. A larger population of high-SFR galaxies with robust wind measurements is clearly needed to test this hypothesis fully.

5 CONCLUSIONS

In this paper, we have presented a spectroscopic catalogue of SMGs and SFRGs at a median redshift of 1.3 that helps us to fill in the *redshift desert* in previous studies of these populations. Redshifts are predominantly measured from [O II] 3727 emission seen in the majority of the spectra and corroborated by various other features corresponding to transitions of Fe II, Mg II, [Ne III], [Ne V], [O III] and the Balmer series. We derive star formation rates from the radio fluxes, stellar masses from a full SED fit and dynamical masses from the [O II] linewidths for these galaxies. In particular we find the following.

(i) SMGs and SFRGs at redshifts of ∼1.3 have lower star-formation rates than those at $z \sim 2$ but are still observed to be in the U/LIRG phase.

(ii) The stellar and dynamical masses of these galaxies show little evolution between redshifts 1 and 2 but are considerably larger than those of optically selected star-forming galaxies at similar redshifts. This lends further support to the premise that these dust-enshrouded galaxies are the progenitors of modern-day ellipticals.

(iii) While the majority of our galaxies have typical spectra for star-forming galaxies, we find significant [Ne III] and [Ne V] emission in just under half of the sample indicating the presence of an AGN. In addition, four galaxies show strong Hδ absorption in addition to [O II] emission indicative of a very dusty starburst.

The [O II] line allows us to define the systemic redshift of the galaxies assuming that the warm ionized gas from which this emission originates is associated with young stars. We look for shifts in interstellar absorption lines relative to [O II] in order to find evidence for large-scale outflows. While most of the individual spectra do not have sufficient S/N for outflow measurements, an analysis of composite spectra yields the following conclusions.

(i) Interstellar absorption lines associated with Mg II and Fe II are found to be at an average blueshift of $-240 \pm 50\,\mathrm{km\,s^{-1}}$ relative to [O II] in SMGs and SFRGs at $z \sim 1.3$.

(ii) SMGs and SFRGs with similar bolometric luminosities are found to drive winds of similar velocities indicating that feedback processes are likely to be comparable in the two populations.

(iii) The outflow velocities in our $z \sim 1.3$ sample are consistent with the $\mathrm{V} \propto \mathrm{SFR}^{0.3}$ relation seen in local ULIRGs and optically selected star-forming galaxies at redshifts around 1.5.

(iv) The average outflow velocities of our SMGs and SFRGs are well explained by a momentum-driven wind model.

We conclude that SMGs and SFRGs at $z \sim 1.3$ allow us to probe a slightly more evolved population than seen at $z \sim 2$. At these redshifts, the galaxies show evidence for cool interstellar outflows as traced by rest-UV absorption lines. Their outflow velocities are found to be similar to those seen in optically selected star-forming galaxies at similar redshifts (which have star formation rates that are

an order of magnitude lower) as well as local LIRGs and ULIRGs (with similar star formation rates). The observations are, however, limited by the relatively poor S/N of individual spectra in the optical/UV as SMGs and SFRGs are highly obscured at these wavelengths. They are however, exceptionally bright in the millimeter wavelengths that trace molecular gas. Detailed hydrodynamic simulations have suggested that galactic winds can entrain large quantities of molecular gas (Narayanan et al. 2008) and this has direct observational consequences for CO morphologies and emission line profiles. There have already been successful attempts at mapping outflows of molecular gas in local ULIRGs (Sakamoto et al. 2009) and the advent of the Atacama Large Millimeter Array (ALMA) will make similar studies possible at high redshifts. In the ALMA era, rest-UV spectroscopic studies of outflows in SMGs and SFRGs will serve as an important benchmark for the millimeter observations allowing comparison of outflows of the low-ionization gas with those of the molecular gas.

ACKNOWLEDGMENTS

The authors thank the anonymous referee for many useful suggestions that have helped improve the paper. We thank James Allen, Paul Hewett, Richard McMahon, Max Pettini, Anna Quider and Vivienne Wild for useful discussions. MB, IS and RJI acknowledge support from STFC. AMS acknowledges support from an STFC Advanced Fellowship. JSD acknowledges the support from the Royal Society via a Wolfson Research Merit Award, and the support from the European Research Council via the award of an Advanced Grant.

REFERENCES

Alatalo K. et al., 2011, ApJ, 735, 88
Alexander D. M., Bauer F. E., Chapman S. C., Smail I., Blain A. W., Brandt W. N., Ivison R. J., 2005, ApJ, 632, 736
Alexander D. M., Swinbank A. M., Smail I., McDermid R., Nesvadba N. P. H., 2010, MNRAS, 402, 2211
Banerji M., Ferreras I., Abdalla F. B., Hewett P., Lahav O., 2010, MNRAS, 402, 2264
Biggs A. D., Ivison R. J., 2006, MNRAS, 371, 963
Binney J., Tremaine S., 1987, Galactic Dynamics. Princeton Univ. Press, Princeton, NJ
Blain A. W., Smail I., Ivison R. J., Kneib J., 1999, MNRAS, 302, 632
Bolzonella M., Miralles J., Pelló R., 2000, A&A, 363, 476
Borys C., Chapman S. C., Halpern M., Scott D., 2002, MNRAS, 330, L63
Bruzual G., Charlot S., 2003, MNRAS, 344, 1000
Carilli C. L., Wang R., 2006, AJ, 132, 2231
Casey C. M. et al., 2009, MNRAS, 399, 121
Casey C. M. et al., 2011, MNRAS, 415, 2723
Chabrier G., 2003, PASP, 115, 763
Chapman S. C., Smail I., Blain A. W., Ivison R. J., 2004, ApJ, 614, 671 (C04)
Chapman S. C., Blain A. W., Smail I., Ivison R. J., 2005, ApJ, 622, 772 (C05)
Chapman S. C. et al., 2010, MNRAS, 409, L13
Cirasuolo M., McLure R. J., Dunlop J. S., Almaini O., Foucaud S., Simpson C., 2010, MNRAS, 401, 1166
Clements D. L. et al., 2008, MNRAS, 387, 247
Coppin K. et al., 2006, MNRAS, 372, 1621
Dye S. et al., 2008, MNRAS, 386, 1107
Erb D. K., Steidel C. C., Shapley A. E., Pettini M., Reddy N. A., Adelberger K. L., 2006, ApJ, 646, 107
Erb D. K., Pettini M., Shapley A. E., Steidel C. C., Law D. R., Reddy N. A., 2010, ApJ, 719, 1168
Faber S. M. et al., 2003, in Iye M., Moorwood A. F. M., eds, SPIE Conf. Ser. Vol. 4841, Instrument Design and Performance for Optical/Infrared Ground-based Telescopes. SPIE, Bellingham, WA, p. 1657
Frye B., Broadhurst T., Benítez N., 2002, ApJ, 568, 558
Genzel R., Baker A. J., Tacconi L. J., Lutz D., Cox P., Guilloteau S., Omont A., 2003, ApJ, 584, 633
Giavalisco M. et al., 2004, ApJ, 600, L93
Gonzalez Delgado R. M., Leitherer C., Heckman T., Lowenthal J. D., Ferguson H. C., Robert C., 1998, ApJ, 495, 698
Hainline L. J., Blain A. W., Smail I., Alexander D. M., Armus L., Chapman S. C., Ivison R. J., 2011, preprint (arXiv:1006.0238)
Heckman T. M., Armus L., Miley G. K., 1990, ApJS, 74, 833
Heckman T. M., Lehnert M. D., Strickland D. K., Armus L., 2000, ApJS, 129, 493
Ivison R. J. et al., 2002, MNRAS, 337, 1
Ivison R. J. et al., 2007, MNRAS, 380, 199
Ivison R. J. et al., 2010, A&A, 518, L31
Kennicutt R. C., Jr, 1998, ApJ, 498, 541
Lehnert M. D., Tasse C., Nesvadba N. P. H., Best P. N., van Driel W., 2011, A&A, 532, L3
Leitherer C., Tremonti C. A., Heckman T. M., Calzetti D., 2011, AJ, 141, 37
Magnelli B. et al., 2010, A&A, 518, L28
Maiolino R. et al., 2008, A&A, 488, 463
Martin C. L., 1999, ApJ, 513, 156
Martin C. L., 2005, ApJ, 621, 227
Morganti R., Tadhunter C. N., Oosterloo T. A., 2005, A&A, 444, L9
Morrison G. E., Owen F. N., Dickinson M., Ivison R. J., Ibar E., 2010, ApJS, 188, 178
Murray N., Quataert E., Thompson T. A., 2005, ApJ, 618, 569
Nagao T., Murayama T., Taniguchi Y., 2001, PASJ, 53, 629
Narayanan D. et al., 2008, ApJS, 176, 331
Neri R. et al., 2003, ApJ, 597, L113
Nesvadba N. P. H. et al., 2007, ApJ, 657, 725
Pettini M., Shapley A. E., Steidel C. C., Cuby J., Dickinson M., Moorwood A. F. M., Adelberger K. L., Giavalisco M., 2001, ApJ, 554, 981
Pettini M., Rix S. A., Steidel C. C., Adelberger K. L., Hunt M. P., Shapley A. E., 2002, ApJ, 569, 742
Poggianti B. M., Wu H., 2000, ApJ, 529, 157
Pope A. et al., 2006, MNRAS, 370, 1185
Rubin K. H. R., Weiner B. J., Koo D. C., Martin C. L., Prochaska J. X., Coil A. L., Newman J. A., 2010, ApJ, 719, 1503
Rupke D. S., Veilleux S., Sanders D. B., 2002, ApJ, 570, 588
Rupke D. S., Veilleux S., Sanders D. B., 2005, ApJ, 632, 751
Sakamoto K. et al., 2009, ApJ, 700, L104
Savage B. D., Sembach K. R., 1991, ApJ, 379, 245
Schwartz C. M., Martin C. L., Chandar R., Leitherer C., Heckman T. M., Oey M. S., 2006, ApJ, 646, 858
Shapley A. E., Steidel C. C., Pettini M., Adelberger K. L., 2003, ApJ, 588, 65
Shi F., Zhao G., Liang Y. C., 2007, A&A, 475, 409
Smail I., Chapman S. C., Ivison R. J., Blain A. W., Takata T., Heckman T. M., Dunlop J. S., Sekiguchi K., 2003, MNRAS, 342, 1185
Snow T. P., Lamers H. J. G. L. M., Lindholm D. M., Odell A. P., 1994, ApJS, 95, 163
Steidel C. C., Erb D. K., Shapley A. E., Pettini M., Reddy N., Bogosavljević M., Rudie G. C., Rakic O., 2010, ApJ, 717, 289
Swinbank A. M., Smail I., Chapman S. C., Blain A. W., Ivison R. J., Keel W. C., 2004, ApJ, 617, 64
Swinbank A. M. et al., 2005, MNRAS, 359, 401
Swinbank A. M., Chapman S. C., Smail I., Lindner C., Borys C., Blain A. W., Ivison R. J., Lewis G. F., 2006, MNRAS, 371, 465
Swinbank A. M. et al., 2008, MNRAS, 391, 420
Swinbank A. M. et al., 2010, MNRAS, 405, 234
Tacconi L. J. et al., 2008, ApJ, 680, 246
Targett T. A., Dunlop J. S., McLure R. J., Best P. N., Cirasuolo M., Almaini O., 2011, MNRAS, 412, 295

Tremonti C. A. et al., 2004, ApJ, 613, 898
Tremonti C. A., Moustakas J., Diamond-Stanic A. M., 2007, ApJ, 663, L77
Wardlow J. L. et al., 2011, MNRAS, 415, 1479
Webb T. M. et al., 2003, ApJ, 587, 41
Weiner B. J. et al., 2009, ApJ, 692, 187
Weiß A. et al., 2009, ApJ, 707, 1201

APPENDIX A: COMPOSITE SPECTRA

In Fig. A1 we present the composite spectra of SMGs, SFRGs as well as galaxies split by their infrared luminosity. In Fig. A2, we show the composite spectra of galaxies split by their [Ne III]/[O II] line ratio as well as the [O II] linewidth which is used to calculate the dynamical mass of the galaxy.

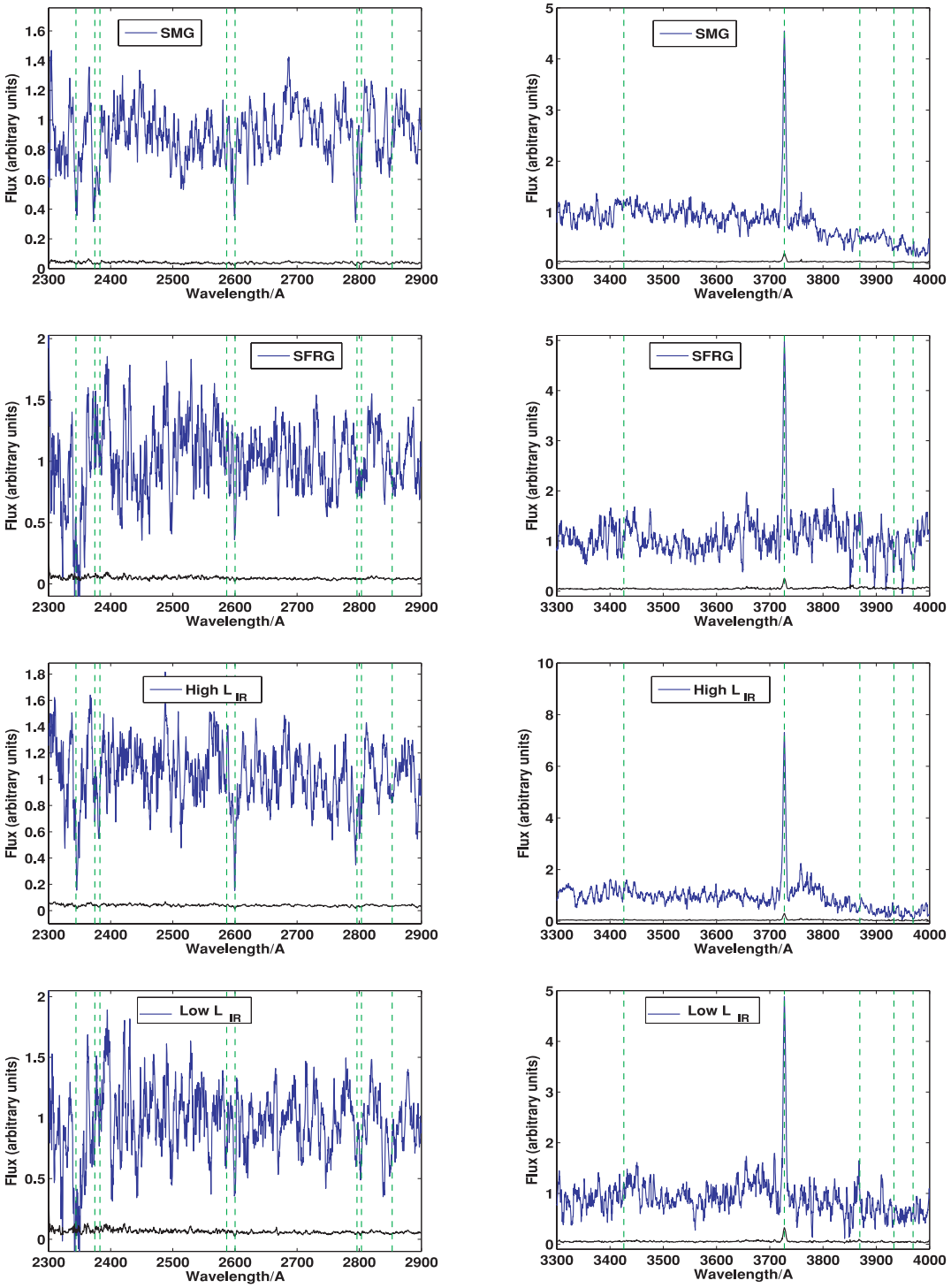

Figure A1. Composite spectra of SMGs, SFRGs and galaxies split by total infrared luminosity in the ISM absorption line region (left) and the [O II] emission line region (right). The error spectrum obtained from jackknife sampling the individual spectra is shown at the bottom of each panel on the same scale. The vertical lines marked are (in order of increasing wavelength) Fe II 2344, 2374, 2383, 2587; Mn II 2594; Fe II 2600; Mn II 2604; Mg II 2796, 2803; Mg I 2853 (left-hand panels) and [Ne V] 3452; [O II] 3727; [Ne III] 3869 and the Ca K&H features at 3933 and 3969 Å (right-hand panels).

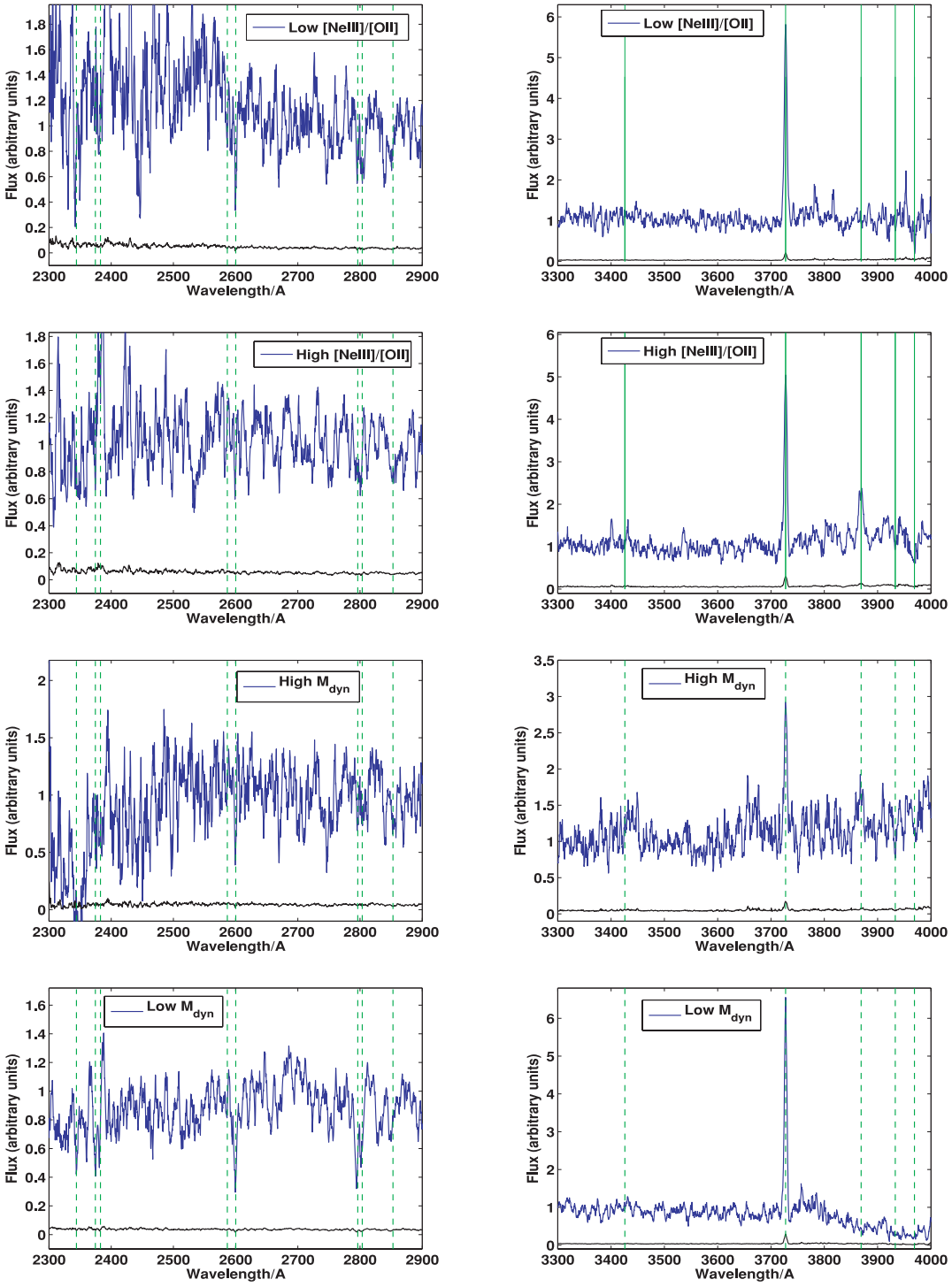

Figure A2. Composite spectra of galaxies split by their [Ne III]/[O II] line ratio as well as dynamical mass in the ISM absorption line region (left) and the [O II] emission line region (right). The error spectrum obtained from jackknife sampling the individual spectra is shown at the bottom of each panel on the same scale. The vertical lines marked are (in order of increasing wavelength) Fe II 2344, 2374, 2383, 2587; Mn II 2594; Fe II 2600; Mn II 2604; Mg II 2796, 2803; Mg I 2853 (left-hand panels) and [Ne V] 3452; [O II] 3727; [Ne III] 3869 and the Ca K&H features at 3933 and 3969 Å (right-hand panels).

This paper has been typeset from a TEX/LATEX file prepared by the author.